Above-Unity Coherent Cooperativity of Tin-Vacancy Centers in Diamond Photonic Crystal Cavities

Nina Codreanu,[1,2,*] Tim Turan,[1,2,*] Daniel Bedialauneta Rodriguez,[1,2,*] Matteo Pasini,[1,2] Lorenzo de Santis,[1,2] Maximilian Ruf,[1,2] Christian F. Primavera,[1,2] Leonardo G. C. Wienhoven,[1,2] Caroline E. Smulders,[1,2] Simon Gröblacher,[2] and Ronald Hanson[1,2,†]

[1]*QuTech, Delft University of Technology, 2628 CJ Delft, The Netherlands*
[2]*Kavli Institute of Nanoscience Delft, Delft University of Technology, 2628 CJ Delft, The Netherlands*

(Received 7 November 2025; accepted 1 April 2026; published 25 June 2026)

The tin-vacancy center in diamond (SnV) has emerged as a compelling building block for realizing next-generation quantum networks thanks to its excellent optical and spin properties. Coupling to photonic crystal cavities (PCCs) promises to further enhance the SnV light-matter interface and unlock a diverse range of entanglement generation protocols. Recent pioneering experiments showing Purcell enhancement of SnV centers in PCCs underscore this potential. However, optical coupling that is coherent—the key ingredient for use in quantum protocols—has so far remained elusive. Here, we demonstrate above-unity coherent cooperativity of SnV centers embedded in photonic crystal cavities. We fabricate free-standing PCCs using a quasi-isotropic undercut. Across two samples, we conduct room-temperature characterizations, measuring resonances for 327 cavities, with an average quality factor exceeding $Q = 1.1(4) \times 10^4$. Two cavity-coupled emitters are examined in detail, exhibiting quality factors up to $Q = 25.4(4) \times 10^3$ and Purcell-reduced lifetimes corresponding to cooperativities up to $C = 20.3(11)$. Furthermore, the single SnVs are observed to strongly modulate the cavity transmission with an extinction contrast up to 98.8(4)%% on resonance. Finally, SnV linewidth measurements reveal above-unity coherent cooperativities in both devices, with the highest value being $C_{\mathrm{coh}} = 8.3(12)$. These results open the door to using cavity-coupled SnV centers as efficient, coherent light-matter interfaces for future quantum networks.

DOI: 10.1103/z514-v4n6

Subject Areas: Nanophysics, Photonics, Quantum Physics

I. INTRODUCTION

A future quantum internet, built using quantum processor nodes connected via optical channels, promises applications such as secure communication, distributed quantum computation, and enhanced sensing [1–3].

Optically active spin qubits in diamond represent a promising building block, with recent demonstrations of multinode quantum networks of remote solid-state qubits [4–9]. One approach to boost the rate of entanglement generation is the integration of diamond spin qubits into nanophotonic devices, such as waveguides and photonic crystal cavities (PCCs) [9–14]. Optical cavities enhance light-matter interactions, increasing the probability of emission into the desired mode to $\beta = C/(C+1)$, which approaches unity at high cooperativities C. In particular, the small mode volumes of PCCs facilitate achieving high cooperativities, leading to high emission efficiencies [15] and opening the door to entanglement schemes in which the devices are operated as spin-photon gates [16].

Tin-vacancy (SnV) centers in diamond have emerged as promising candidates to implement quantum networking hardware due to their favorable optical and spin properties. Recent experiments have demonstrated their suitability as quantum network nodes, including high-fidelity control of the electron spin [17–19], the use of nearby ^{13}C nuclear spins as memory qubits [20,21], hybrid integration with photonic chips for routing [22–24], strain tuning of the SnVs emission frequency [25,26], two-photon quantum interference of emitted photons [27,28], and their conversion to the telecom band [29]. Moreover, multiple works have shown cavity-coupled SnVs with cooperativities up to $C \approx 15$ [14,30,31].

In this work, we report on the fabrication of diamond photonic crystal cavities. We first characterize a subset of the fabricated devices in a room-temperature setup

[*]These authors contributed equally to this work.
[†]Contact author: R.Hanson@tudelft.nl

(Appendix A), obtaining statistics on their quality factors and resonance frequencies. At cryogenic temperatures (Appendix B), cavity-coupled SnV centers are identified through *in situ* frequency tuning using nitrogen gas deposition [32,33]. We then focus on two cavities, for which we measure both C and C_{coh}. The coherent cooperativity C_{coh} quantifies the enhancement of the light-emitter interaction, including dephasing, and it is a key figure of merit determining the fidelity of entanglement schemes [34]. So far, reaching $C_{\mathrm{coh}} > 1$ for cavity-coupled SnVs has remained elusive. Here, we measure a Purcell-reduced lifetime corresponding to $C = 20.3(11)$ and an emitter-modulated cavity transmission, obtaining $C_{\mathrm{coh}} = 8.3(12)$.

II. DESIGN AND FABRICATION

A schematic illustration of our photonic crystal cavities is shown in Fig. 1(a). The devices are single-sided photonic crystal cavities, consisting of a strong mirror, a central cavity region, and a weak mirror [35]. For both strong and weak mirrors, we use the same lattice constant a_n (Appendix C). The total cavity decay rate $\kappa = \kappa_e + \kappa_i$ is divided into an external part κ_e that is guided by the diamond waveguide and an internal part κ_i that contains all other decay channels. Figure 1(b) shows a finite element method (FEM) simulation of the electric field strength of the cavity mode. The highest cooperativity is achieved for a SnV center located at its maximum. Figure 1(c) illustrates a simplified level structure of the SnV-cavity system, with rates indicated by arrows and energies by dotted lines.

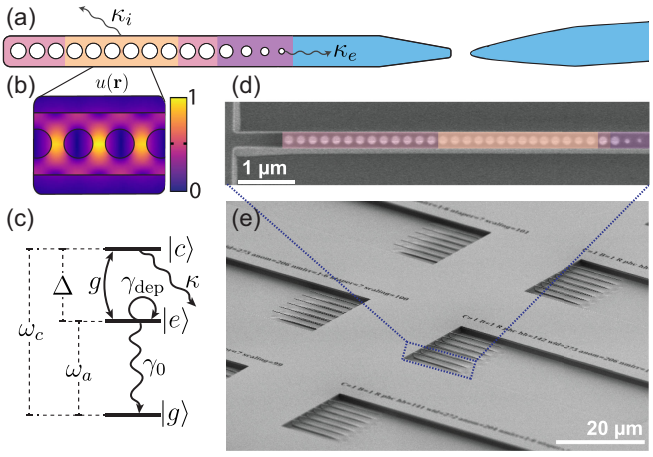

FIG. 1. Tin-vacancy centers in diamond PCCs. (a) Schematic of the device. The PCC design is illustrated from left to right: strong mirror, defect region, weak mirror, and taper end. We collect the light with a tapered optical fiber in a lensed configuration. (b) Simulated electric field of the fundamental cavity mode normalized to the maximum $u(\mathbf{r})$ (see Appendix G). (c) Simplified level structure of the combined emitter-cavity system. The emitter is described by a transition frequency ω_a between the ground state $|g\rangle$ and the excited state $|e\rangle$. The spontaneous emission rate is denoted γ_0, and γ_{dep} is the dephasing rate. The state $|c\rangle$ denotes a photon in the cavity mode and the emitter in the ground state. The cavity mode has a tunable frequency $\omega_c = \omega_a + \Delta$, and its total decay rate is $\kappa = \kappa_i + \kappa_e$. The coupling strength between the cavity and the emitter is g. (d) SEM image of a free-standing PCC, taken at a 0° angle. The device regions (false colored) correspond to the schematic in panel (a). (e) SEM image of the diamond sample taken at a 65° angle. It displays multiple arrays of cavities, each containing six PCCs.

The realization of SnV center integrated devices is described in two main steps: First, the SnV centers are created via ion implantation and high-temperature, low-pressure annealing; second, photonic crystal cavity devices are fabricated via the quasi-isotropic etch undercut method [22,30,36–39].

Starting from a bulk diamond, the integration of SnV centers in diamond substrates follows the methods described in Appendix D. We incorporate ^{120}Sn ions in the diamond substrate via high-energy ion implantation (350 keV, 7° implantation angle), resulting in an implantation depth of 88 nm ± 16 nm. This approach places the ions close to the vertical maximum of the cavity mode. The SnV centers are activated via high-temperature, low-pressure annealing (1100 °C for a duration of 4 hours) by the surface-protected annealing method [40].

The device fabrication follows by patterning the Si_xN_y hard mask material, followed by the transfer pattern into the diamond substrate and vertical coverage with AlO_x of the structures' sidewalls. Next, the devices are undercut by employing the quasi-isotropic etch (QIE), followed by an upward etch to thin the devices to a thickness of around 180 nm. Fabrication concludes with an inorganic removal of the hard mask materials. An exemplary fabricated cavity is shown in Fig. 1(d). Complementary scanning electron microscopy (SEM) and atomic force microscopy (AFM) inspection of representative devices (Appendix E) allow us to infer the device geometry, confirming a high degree of control over the fabrication process. The cavities are grouped in arrays of six devices each, as shown in Fig. 1(e). Within each cavity array, we sweep the number of holes in the weak mirror region (from one to six) to vary the cavity out-coupling κ_e.

III. DEVICE CHARACTERIZATION

The device characterization is performed first at room temperature by contact coupling a tapered optical fiber and probing the cavities' spectra in reflection with a supercontinuum white laser. The reflection spectrum for a specific cavity (called Cavity 1 from here on) is shown in Fig. 2(a). Additionally, we show the Gaussian IRF of the spectrometer. The IRF is measured by leaking a resonant laser into the spectrometer. The spectrum is fitted by a Lorentzian with linear background convolved with the IRF, and the quality factor is obtained as $Q = \lambda_c/\Delta\lambda$. We present fabrication results for two distinct diamond samples and compare their quality factor distributions. For Sample 1, of the 232 investigated devices, 200 show a resonance.

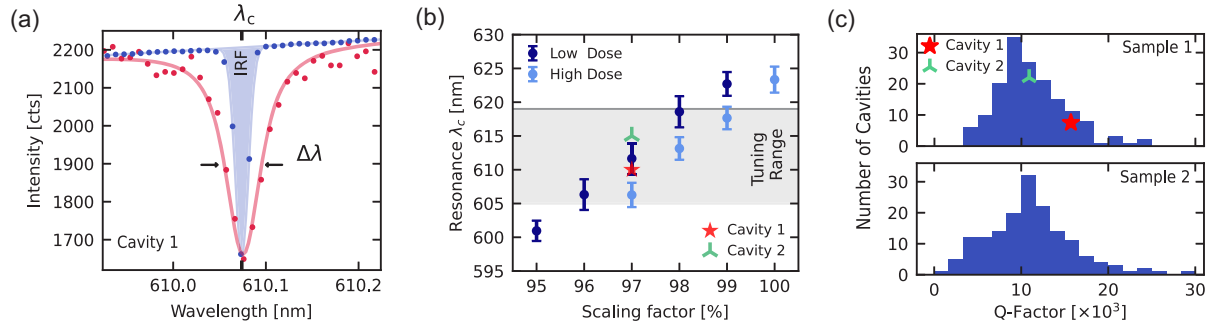

FIG. 2. Room-temperature PCC characterization. (a) Resonance of Cavity 1 measured by taking a reflection spectrum. The spectrum is fitted with a Lorentzian plus linear background convolved with the spectrometer instrument response function (IRF). From the fit, we determine the quality factor $Q = \lambda_c/\Delta\lambda$. (b) Cavity resonance vs device scaling factor for Sample 1. We vary the geometrical parameters of the cavities by a common scaling factor, changing the hole diameter, lattice constant, and device width. Devices within the indicated tuning range can be brought into resonance with the SnVs zero-phonon line at 619 nm by gas deposition (Appendix H). We use two different e-beam exposure doses, 265 $\mu C/cm^2$ and 275 $\mu C/cm^2$ (dark and light blue). The error bars indicate $\pm 1\sigma$ of the distribution of resonances. (c) Distribution of all quality factors for Sample 1 (top panel) and Sample 2 (bottom panel). The average quality factor is $Q = 1.1(4) \times 10^4$. The measured quality factors of Cavity 1 and Cavity 2 are $Q = 15.7(10) \times 10^3$ and $Q = 10.9(5) \times 10^3$, respectively.

Similarly, in Sample 2, it is 216 out of 254 devices. This result corresponds to a fabrication yield of about 85% for both samples. We report on 327 quality factors in total (Appendix F).

A small variability in the fabrication process can cause large shifts in the cavities' resonance frequencies. To guarantee there will be cavities with resonances close to the SnV zero-phonon line (ZPL) at 619 nm, we sweep the cavity design by varying a scaling factor (lattice constant a_n, waveguide width w_{wg}, and hole radius r). Figure 2(b) shows the cavity resonances as a function of this scaling factor for Sample 1. The nominal design parameters (scaling factor of 100%) show a cavity resonance slightly exceeding 620 nm, in good agreement with FEM simulations (Appendix G). Specifically, devices with a scaling factor from 95% to 99% show a cavity resonance blue detuned with respect to the SnV ZPL, allowing for gas tuning of the cavity resonance (Appendix H).

Additionally, for Sample 1, we use two electron beam (e-beam) exposure doses. We find that devices patterned with a higher dose (275 $\mu C/cm^2$, light blue) show, on average, a 5 nm lower cavity resonance than the devices exposed to a lower dose (265 $\mu C/cm^2$, dark blue). We expect devices exposed to the higher dose to have a systematically larger hole diameter and smaller cavity width, explaining the slight shift in resonance frequency. Other parameters, such as lattice constant and cavity thickness, are presumably not affected.

Thus, we see a high sensitivity of the cavity resonance to a small variation of the process parameters, demonstrating that a high degree of control over the fabrication process is required to ensure high accuracy over the target cavity resonance. Two cavities are marked and investigated in more detail in the later sections of this work. Both cavities are exposed to the low dose.

Figure 2(c) shows the distribution of quality factors for Sample 1 (top) and Sample 2 (bottom). The average quality factor for both samples is $Q = 1.1(4) \times 10^4$. No significant dependence is observed between the quality factor and the scaling factor. The measured quality factors are lower than simulated due to fabrication imperfections such as sidewall and bottom surface roughness (Appendix G). Both samples show a similar distribution of quality factors, demonstrating the reproducibility of the proposed fabrication methods.

These results show that the developed fabrication process is characterized by a high control over the process parameters and that it systematically yields high-performance cavity devices.

IV. CAVITY-EMITTER COUPLING

The Purcell-reduced lifetime of an emitter in an optical cavity is given by

$$\tau = \frac{\tau_0}{Cf(\Delta) + 1}, \tag{1}$$

where $f(\Delta) = 1/(1 + 4\Delta^2/\kappa^2)$ is the spectral mismatch factor, $\Delta := \omega_c - \omega_a$ is the detuning between the cavity and the emitter, and τ_0 is the natural lifetime. The cooperativity C follows,

$$C = F_p \beta_0 u^2(\mathbf{r}) \zeta, \tag{2}$$

where $F_p = [3/(4\pi^2)](\lambda/n)^3(Q/V)$ is the Purcell factor, V is the mode volume, $u(\mathbf{r}) \in [0, 1]$ is the normalized field strength at the emitter location, and ζ is the polarization mismatch. The factor $\beta_0 = 0.8 \times 0.56 \times 0.8 = 0.36$ is the product of quantum efficiency [41], the Debye-Waller factor [42], and the branching ratio [30]. The SnV transition dipole is oriented along the diamond's $\langle 111 \rangle$ crystallographic

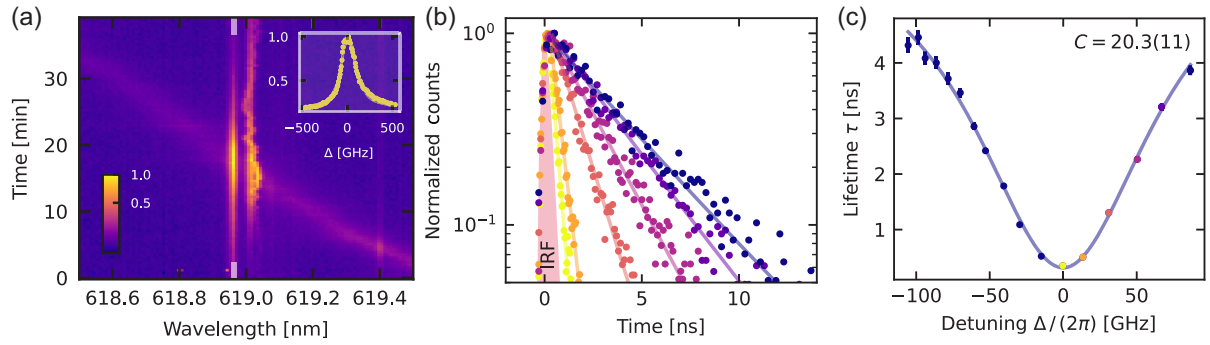

FIG. 3. Cavity-emitter coupling. (a) Detected counts on a spectrometer as the cavity is tuned. This experiment is used to identify cavity-coupled SnVs. Initially, the cavity resonance is shifted to about 619.5 nm using gas deposition. Then, the cavity is tuned backwards by evaporating the deposited nitrogen with a green laser. When the cavity is on resonance with the SnV, it increases in brightness (indicated by the gray marks). The inset shows the spectrometer counts at this frequency (618.96 nm) as a function of cavity detuning Δ. (b) SnV excited off resonantly with a pulsed green laser. The collected ZPL counts are measured with an APD and recorded on a time tagger. The result is fitted with a single exponential decay to obtain the lifetime τ. (c) Lifetime as a function of detuning fitted with $\tau = \tau_0/(Cf(\Delta)+1)$, leading to $C = 20.3(11)$. The error bars indicate $\pm 1\sigma$ uncertainty of the single exponential fit.

axis, whereas the cavities are oriented along one of the $\langle 110\rangle$ axes. At the field's maximum, $\zeta = 2/3$ (Appendix G). The value of $u(\mathbf{r})$ is randomly distributed, due to the blanket implantation used in this case.

To find an SnV that is coupled to the cavity, we perform the measurement shown in Fig. 3(a). First, the sample is cooled down in a cryostat to 9 K. We then introduce a small amount of nitrogen gas into the vacuum chamber (Appendix H). The gas deposits on the PCC and shifts the cavity resonance λ_c. We stop the process slightly red detuned from the SnV ZPL. Then, we measure spectra alternating between excitation with the white laser and the green laser, both delivered from the top through an objective. A fraction of the light is scattered into the cavity and then collected with a tapered fiber [Fig. 1(a)]. With the white laser, we measure λ_c, and the green laser (4.5 mW, 10 s per step) back tunes the cavity and off resonantly excites the SnVs. A cavity-coupled SnV will increase in brightness when in resonance with the cavity. This measurement was performed on nine cavities in Sample 1, of which seven showed cavity-coupled emitters. The data shown in Fig. 3(a) belong to Cavity 2, and the line with gray marks corresponds to emitter 2. The other visible lines are presumably different SnVs.

After identifying a cavity-coupled SnV, we measure its Purcell-reduced lifetime τ to obtain the cooperativity C. In Fig. 3(b), we again tune the cavity, this time using less green laser power (2.7 mW, 1 s each step) to achieve smaller frequency steps. At each step, the SnV is excited with a pulsed green laser (70 ps pulse length), and the ZPL emission is recorded on a time tagger. We spectrally filter the collected signal to isolate the ZPL of the SnV under investigation (Appendix B). The measured counts are fitted with a single exponential decay to obtain the lifetime. In this case, the smallest value is $\tau_{\mathrm{min}} = 0.32(1)$ ns. We perform a convergence test to confirm that the IRF does not significantly influence the measured lifetime (Appendix I).

Figure 3(c) shows all measured lifetimes as a function of the cavity-emitter detuning $\Delta = \omega_c - \omega_a$. The data are fitted with $\tau = \tau_0/(Cf(\Delta)+1)$, obtaining $\tau_0 = 6.9(4)$ ns and $C = 20.3(11)$. Figures 3(b) and 3(c) belong to Cavity 1.

These results show a cavity-coupled SnV, with a strongly Purcell-reduced lifetime. However, lifetime measurements are insensitive to dephasing effects. To further probe the coherence of this light-matter interface, we perform resonant measurements of the same SnV in the next section.

V. COHERENT INTERACTIONS

Dephasing is an important factor in predicting the performance of a cavity-emitter system for entanglement protocols [43]. While the cooperativity $C = [(4g^2)/(\kappa\gamma_0)]$ quantifies the cavity-enhanced decay rate of the emitter over its natural linewidth γ_0, the coherent cooperativity $C_{\mathrm{coh}} = [(4g^2)/(\kappa\gamma)]$ depends on the off-resonant linewidth γ. Here, g is the emitter-cavity coupling, and $\gamma = \gamma_0 + \gamma_{\mathrm{dep}}$ is the off-resonant emitter linewidth including dephasing.

In Fig. 4, we probe coherent cavity-emitter interactions by scanning a laser across the cavity (20 s per scan). The cavity is illuminated from the top with around 120 pW of red laser light (Appendix B). Some of the light is scattered into the cavity, collected via the tapered fiber, and split into a ZPL and a phonon side band (PSB) using a dichroic mirror [Fig. 4(a)]. We measure the Purcell-broadened linewidth γ' of the emitter in the PSB. The PSB signal shown in Fig. 4(b) is relatively weak due to the cavity being in resonance [see discussion below for Fig. 4(e)]. We refer to the signal in the ZPL as cavity transmission. Solving the Hamiltonian of the system in the weak excitation regime (Appendix J) gives an analytical expression for the transmission,

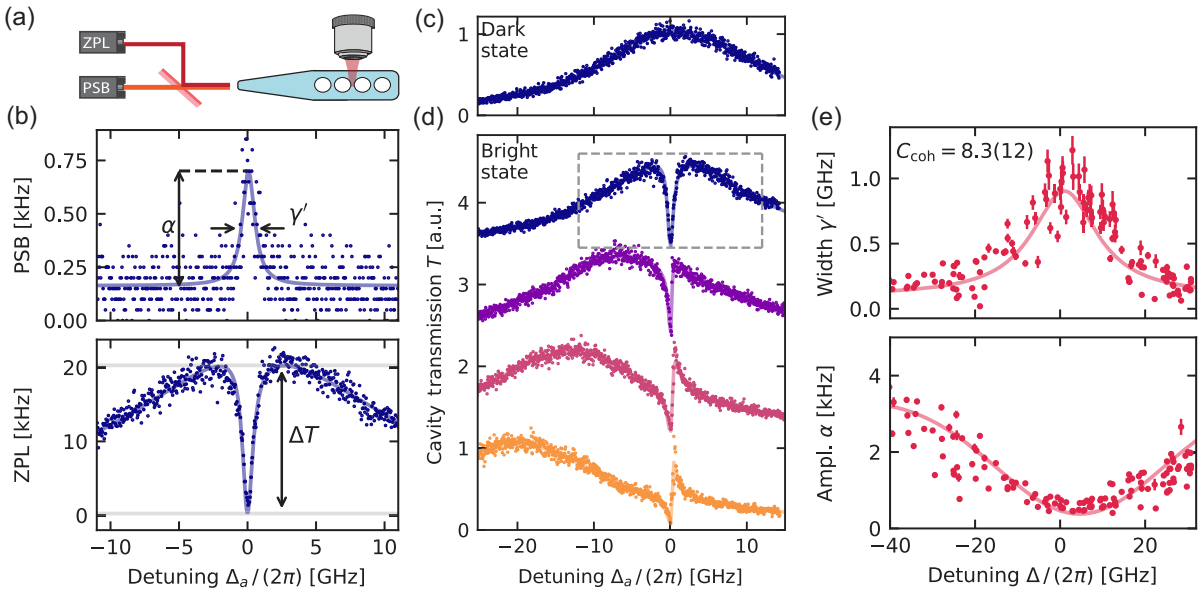

FIG. 4. Coherent SnV-cavity interactions. (a) Collected light split into ZPL and PSB using a dichroic mirror. (b) Cavity and SnV tuned on resonance, where $\Delta \coloneqq \omega_c - \omega_a = 0$. The red laser is scanned across the cavity resonance; PSB and ZPL are recorded as a function of the laser-SnV detuning $\Delta_a \coloneqq \omega - \omega_a$. The top panel shows the collected PSB counts: a Purcell-broadened line shape that is fitted by a Lorentzian with amplitude α and linewidth γ'. The bottom panel shows the cavity transmission. For this detuning, Eq. (3) predicts a symmetric dip. Fitting the data reveals a contrast of $\Delta T = 0.988(4)$. (c) Lorentzian transmission of a bare cavity, where $Q = 25.4(4) \times 10^3$, when the SnV is in a dark state. (d) Cavity transmission modulated by the interaction with the emitter [15] when the SnV is in the bright state. The transmission is shown for four different detunings, $\Delta \in [0, 5, 12, 20]$ GHz. (e) Emitter linewidth γ' as a function of detuning (top panel). Because of the Purcell effect, the linewidth broadens as the emitter and cavity are tuned on resonance. The data are fitted with $\gamma' = \gamma(f(\Delta)C_{\mathrm{coh}} + 1)$ and yield $C_{\mathrm{coh}} = 8.3(12)$. Conversely, the bottom panel shows that the amplitude α decreases. This result can be explained by a lower excited-state population on resonance (Appendix J). The error bars indicate $\pm 1\sigma$ uncertainty of the fits. All data belong to Cavity 1.

$$T(\omega) = \left| \frac{\sqrt{\kappa_{\mathrm{in}}\kappa_e}}{\kappa/2 + i(\omega - \omega_c) + \frac{g^2}{\gamma/2 + i(\omega - \omega_a)}} \right|^2, \qquad (3)$$

where ω_c, ω_a, and ω are the frequencies of the cavity, atom, and probe laser, respectively [15], and κ_{in} is the laser excitation rate of the cavity mode from the top. Figure 4(b) shows the emitter line shape (top) and cavity transmission (bottom) when the emitter and cavity are on resonance ($\Delta = 0$). We find a transmission dip contrast of $\Delta T = 0.988(4)$, a significant improvement over the 0.25 previously measured with a waveguide-coupled SnV [11] and the 0.5 measured in an open microcavity [31].

Before each laser scan, we apply a 100 μs green laser pulse. This pulse probabilistically initializes the SnV to the bright SnV^- state. Conversely, the green pulse can also ionize the SnV^- into a dark state [45]. We use the PSB signal to discern whether the SnV is in a dark or a bright state. In a dark state [Fig. 4(c)], we observe the response of the bare cavity. Fitting a Lorentzian yields the quality factor $Q = 25.4(4) \times 10^3$. The quality factor measured this way is consistent with the spectrometer measurements for Cavity 2, but for Cavity 1, it is higher. We attribute this change to frequency tuning, as we have observed that nitrogen deposition can both increase and decrease the quality factor.

In the bright state, the cavity transmission is modulated by the emitter. Figure 4(d) shows the cavity transmission for four different detunings, $\Delta \in [0, 5, 12, 20]$ GHz, where the $\Delta = 0$ case corresponds to Fig. 4(b) (dashed rectangle).

In Fig. 4(e), the linewidths γ' of the PSB signal are plotted as a function of detuning and fitted with $\gamma' = \gamma(f(\Delta)C_{\mathrm{coh}} + 1)$. This plot reveals cavity quantum electrodynamics (C-QED) parameters $\{g, \kappa, \gamma\}/2\pi = \{1.94(8), 19.0(3), 0.097(4)\}$ GHz, yielding a coherent cooperativity of $C_{\mathrm{coh}} = 8.3(12)$. The emitter presents additional broadening compared to the natural linewidth of $\gamma_0 = 2\pi \cdot 24(1)$ MHz likely due to a combination of dephasing and temperature broadening. At the temperature of the experiment (9 K), a linewidth 2 to 3 times broader than the lifetime limit is expected [46]. Reduced temperature broadening alone would roughly double C_{coh} if the experiment were performed at 4 K. The amplitude α of the PSB signal decreases when the emitter and the cavity are on resonance, which is a result of a decrease in the steady-state population of the emitter's excited state due to an increased decay rate into the cavity at resonance. We fit the data with an envelope of the scattering intensity (Appendix J). For the fit in the bottom panel of Fig. 4(e), we fix g, κ, and γ_0 to the measured values and leave a proportionality constant and the center of the curve free.

We attempted to measure the coherent cooperativity for a total of four SnVs in four different cavities. The emitters were investigated because they increase in brightness when on resonance with the cavity, as shown in Fig. 3(a). Of the four emitters, one showed no transmission dip, one showed a slight dip ($C_{\mathrm{coh}} \approx 0.2$), and the last two, Cavity 1 and Cavity 2, showed significant dips with $C_{\mathrm{coh}} = 8.3(12)$ and $C_{\mathrm{coh}} = 1.6(2)$, respectively. The large variance is likely due to the random position of the SnV within the cavity mode, quantified by $u(\mathbf{r})$. Together with a laser scan in reflection (Appendix K) to measure κ_e, this section completes a full investigation of C-QED parameters (Appendix L). All measurements from the main text are repeated for Cavity 2 (Appendix M).

VI. PERFORMANCE CHARACTERISTICS

An important performance characteristic for cavity-enhanced light-matter interfaces is the external beta factor $\beta_e = (\kappa_e/\kappa)[C/(C+1)]$. It is the probability that an excited emitter will emit into the cavity mode and that this emitted photon will leave the cavity through the out-coupling mirror. In Fig. 5(a), we plot β_e as a function of the factor $u^2(\mathbf{r}) \times \zeta$ (see Appendix G), which effectively links the emitter's location with the cavity-emitter coupling g for a fixed cavity design. We use this approach for two external couplings, $\kappa_e/\kappa \in \{0.21, 0.31\}$, which correspond to Cavity 1 and Cavity 2, respectively. For each curve, we mark the investigated emitters. In both cases, further improving the emitter location would not have a large effect on β_e because $C/(C+1)$ is already close to 1. However, increasing the out-coupling κ_e/κ would also increase β_e in the limit of well-positioned emitters.

In Fig. 5(b), we illustrate how β_e depends on the internal and external cavity losses. The external loss κ_e is a parameter that can be chosen by design: The fewer the holes in the weak mirror region, the larger κ_e. Increasing κ_e will increase the ratio of photons leaving the cavity through the weak mirror κ_e/κ. Simultaneously, it will decrease the quality factor Q and thus the probability β of emitting into the cavity mode ($C \propto F_p \propto Q \propto 1/\kappa$). In effect, there is an optimum κ_e for a fixed κ_i [44]. Specifically for emitter 1, $\kappa_e/\kappa = 0.83$ would result in $\beta_e = 0.67$. The internal loss κ_i can be seen as a gauge for how well the cavity is designed and fabricated, and decreasing κ_i will always result in a higher β_e. In Fig. 5(b), we also show iso-lifetime curves for an emitter with $\tau_0 = 6.5$ ns. Short lifetimes increase the complexity of emission-based experiments due to a trade-off between short excitation pulses and the optical selectivity of the spin states. For emission-based entanglement experiments, the β_e of around 0.24 of emitter 2 would already yield a significant efficiency improvement compared to the β_e of reported SnV-waveguide devices [11].

The external coupling κ_e/κ is also an important parameter for entanglement protocols that rely on the reflection from the cavity. In Fig. 5(c), we show the calculated reflection for Cavity 1 for different emitter frequencies. We use the C-QED parameters of emitter 1. For recently proposed protocols [8], the entanglement fidelity is directly dependent on how small the reflection at the emitter dip is. It can be mathematically proven that there always exists a cavity-emitter detuning for which the dip goes to zero as long as the cavity is overcoupled, i.e., $\kappa_e/\kappa > 0.5$. This case is illustrated in Fig. 5(c), where we see that it is not possible to reach a dip to zero for the out-coupling of 0.21.

VII. OUTLOOK

The presented cavities reach coherent cooperativities compatible with quantum networking protocols [8,47]. However, several opportunities remain to further enhance device performance. Increasing the out-coupling κ_e/κ

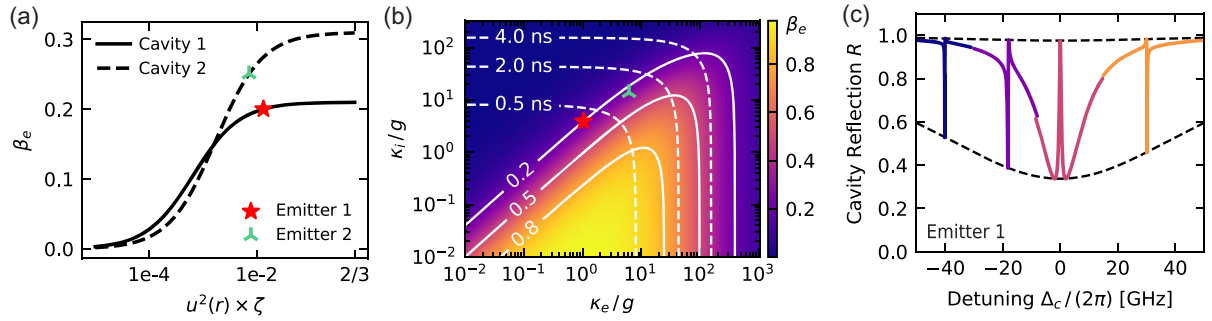

FIG. 5. Influence of the external coupling. (a) External beta factor $\beta_e = (\kappa_e/\kappa)[C/(C+1)]$ as a function of the emitter location for two different external couplings, $\kappa_e/\kappa \in \{0.21, 0.31\}$, corresponding to Cavity 1 and Cavity 2. Within each curve, we mark the point corresponding to the investigated emitters. (b) External beta factor as a function of the loss rate into the waveguide κ_e and other losses κ_i. The dashed lines indicate Purcell-reduced lifetimes of 0.5, 2, and 4 ns relative to a natural lifetime of $\tau_0 = 6.5$ ns. The solid lines mark external beta factors of 0.2, 0.5, and 0.8. A similar plot for the silicon vacancy center (SiV) can be found in Ref. [44]. (c) Calculated cavity reflection as a function of laser-cavity detuning Δ_c for four different emitter frequencies. The solid lines correspond to the emitters' response, similar to those found in Fig. 4(d), but in reflection. The dashed black lines mark the envelope of the peaks and the dips. We use the C-QED parameters of emitter 1.

would benefit both emission-based and reflection-based entanglement protocols. Specifically, a cavity with the same internal loss as presented here could reach external beta factors as high as $\beta_e = 0.67$ when κ_e is optimally chosen. Increasing κ_e can be achieved by further removing unit cells or by using alternative cavity designs [44,48]. Alternatively, fabricating cavities with smaller internal losses κ_i makes it possible to achieve overcoupled cavities without compromising their quality factor Q [12]. Emerging diamond fabrication processes [49] result in ultralow surface roughness of the device layer [50] and demonstrate the highest optical quality factors to date [12,51].

Using adiabatic fiber coupling instead of lensed fiber coupling could increase the photon collection roughly threefold [11,52]. To successfully implement this method, the device containing the SnV center must be mechanically isolated from the coupling fiber and the fiber must be fully thermalized to the sample temperature. Finally, methods such as focused ion beam (FIB) implantation [53] and masked implantation [54] can be implemented to gain more control over the position of the SnV within the cavity mode. These methods prevent the formation of SnVs in the low cooperativity regions of the device. Moreover, FIB implantation with sufficient accuracy and precision [55] enables positioning the SnVs close to the mode maximum, thereby yielding higher and more consistent cooperativities.

In addition to these improvements, supplementing the current results with capabilities established in other work will enable the operation of a complete quantum network node. Spectral diffusion can be mitigated by implementing charge-resonance (CR) checks [56]. High-fidelity electron spin control can be achieved by microwave driving [17–19,21]. For the SnV, the presence of strain is required to enable efficient microwave driving. Future research is needed to establish whether the fabrication-induced strain in the presented devices is sufficient for fast spin control or whether an active straining method is desired [17]. In the latter case, the cavity design could also be adapted from hole based to corrugated [48,57] to achieve large and tunable strain.

Combining these improvements would give us access to a parameter regime with near-unity external coupling factors β_e while retaining spin-selective excitation. Such a device would enable various applications, such as high-rate entanglement distribution or the (near-)deterministic creation of multidimensional cluster states [58].

ACKNOWLEDGMENTS

We thank Julius Fischer, Yanik Herrmann, and Niv P. Bharos for helpful and important discussions, Henri Ervasti for software support, Hans K. C. Beukers and Christopher Waas for help with measurement scripts, Julia M. Brevoord and Alexander M. Stramma for help with the cryogenic setup, and Julius Fischer and Yanik Herrmann for proofreading the manuscript. We acknowledge financial support from the joint research program "Modular Quantum Computers" by Fujitsu Limited and Delft University of Technology co-funded by the Netherlands Enterprise Agency under Project No. PPS2007, the Dutch Research Council (NWO) through the Spinoza prize 2019 (Project No. SPI 63-264), the Dutch Ministry of Economic Affairs and Climate Policy (EZK) as part of the Quantum Delta NL program, the Quantum Internet Alliance through the Horizon Europe program (Grant Agreement No. 101080128), and The Kavli Foundation through the Kavli Institute Innovation Award "Quantum Materials for Broad-Band Quantum Transduction".

N. C., T. T., and D. B. R. contributed equally to this work. N. C., M. R., and L. D. S. designed the devices. N. C. developed and optimized the device fabrication process with assistance from M. R. and S. G. N. C. fabricated the devices and tapered fibers, with assistance from L. G. C. W. and C. E. S. N. C. and M. P. designed the room-temperature setup, and N. C. and L. D. S. built it. N. C. conducted the room-temperature experiments, and N. C. analyzed the data with help from T. T. M. P. and T. T. built the cryogenic setup. T. T. built and tested the gas tuning system. T. T. and D. B. R. conducted the cryogenic experiments and analyzed the data. D. B. R. and T. T. modeled the fabricated devices. C. F. P. characterized the diamond samples before fabrication. N. C., T. T., D. B. R., and R. H wrote the manuscript with input from all authors. R. H. supervised the experiments.

DATA AVAILABILITY

The data that support the findings of this article are openly available [59].

APPENDIX A: ROOM-TEMPERATURE SETUP

A schematic of the room-temperature, single-sided cavity device characterization setup is shown in Fig. 6.

The diamond sample is mounted (via carbon tape) on the sample stage, positioned on top of the XY piezo positioner stack (Smaract MCS2-S), allowing sample position control in the XY direction. The tapered optical fiber is mounted on a variable angle (manually set) stage, mounted on a slip-stick Z piezo positioner (Smaract MCS2-S), which allows one to control the vertical position of the fiber.

The sample is imaged by illuminating it with a LED at around 470 nm using a microscope objective [100X, numerical aperture (NA) 0.8], coupled to a digital camera (CS165CU/M, Thorlabs). This approach provides enough resolution to optically resolve both the optical fiber tip and the free-hanging, device-coupled, tapered waveguide cavity.

The input broadband laser light source (SuperK Compact, NKT Photonics supercontinuum white light source) is

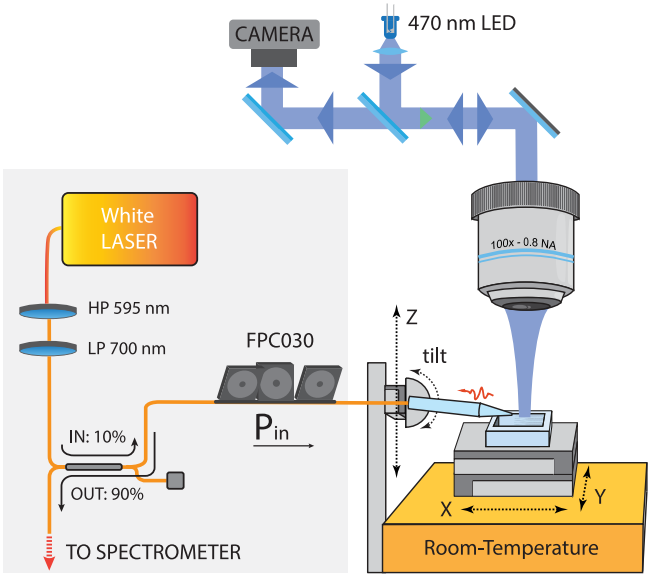

FIG. 6. Room-temperature characterization setup.

spectrally filtered using a long-pass and a short-pass filter, resulting in a probe spectrum spanning 595 nm to 700 nm. A 90:10 beam splitter is used to send 10% of the laser light to the input fiber, where we use a Fiber Polarization Controller (FPC030 by Thorlabs) to vary the polarization and match it to the device polarization (set by geometry). The probe light is delivered adiabatically via the contact-coupled tapered optical fiber. It couples to the single-sided cavity via the weak mirror region and is reflected back to the same fiber port. The reflected signal (90%) is then sent to the spectrometer (SpectraPro HRS-500).

APPENDIX B: CRYOGENIC SETUP

Figure 7 shows a sketch of the measurement setup. The diamond sample is cooled to around 9 K in a closed-cycle cryostat (Montana Instruments s50). The usual 4 K base temperature of the s50 is not reached because the N_2 gas line (Quantum Design, MI-4100-1184) is inside the heat-shield and not thermalized to the 40 K stage. This result can

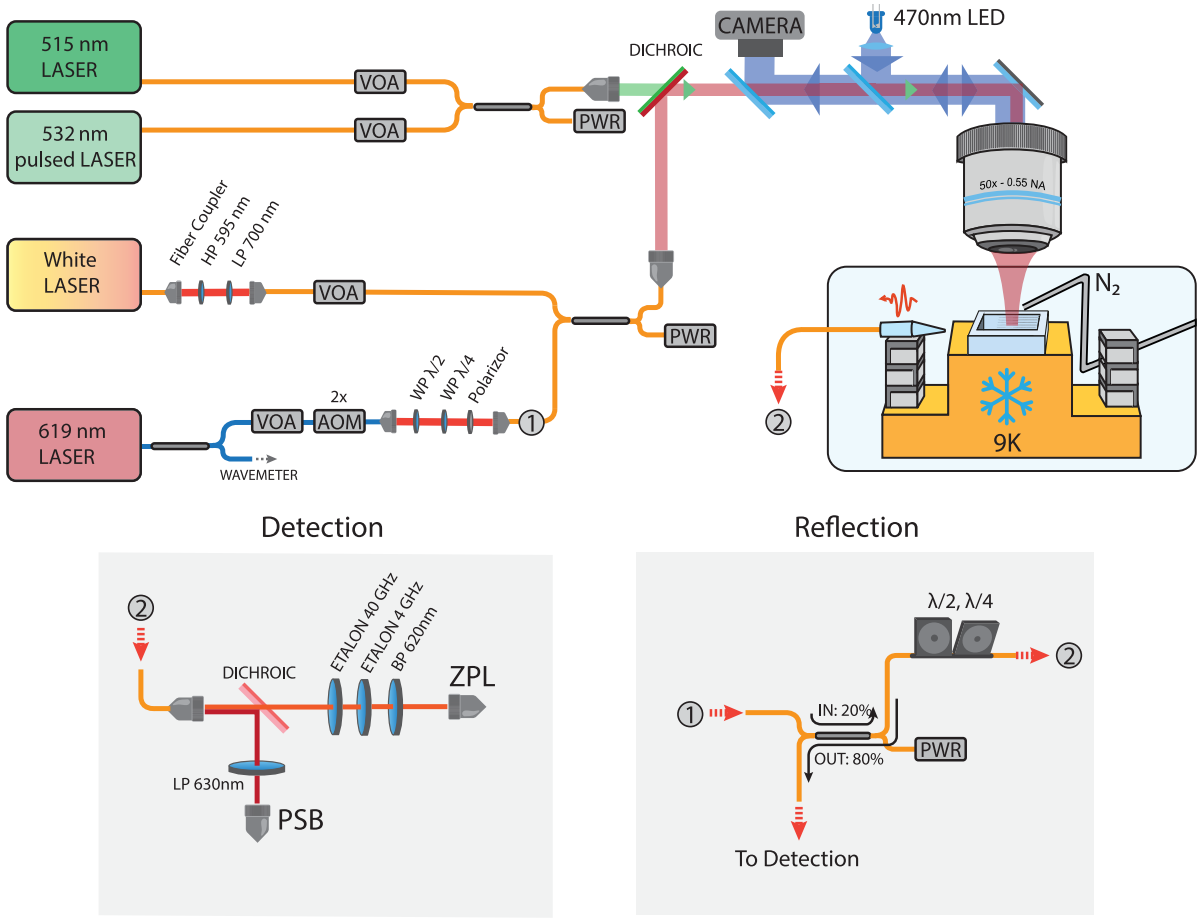

FIG. 7. Measurement setup. The laser powers are controlled via variable optical attenuators (VOA, Thorlabs VOA630PM-APC) and calibrated using power meters (PWR, Thorlabs S120C). The 619 nm laser can be pulsed with an acousto-optical modulator (AOM, Gooch & Housego Fiber-Q). For all experiments in the main text, the PCCs are measured via top excitation, where the tapered fiber is directly connected to the detection setup shown in the bottom left. For the reflection measurements (Appendix K), the setup shown in the bottom right is plugged in between the red laser and the detection setup.

TABLE I. Cavity design parameters.

Parameter	Symbol	Value
Lattice constant	a_n	206 nm
Hole radius	r	71 nm
Width	w_{wg}	275 nm
Thickness	t_h	230 nm
Fractional deviation	d	0.1
Slope well function	η	1.05
Unit-cell defect region	N	7
Unit-cell strong mirror	M_s	13
Unit-cell weak mirror	M_w	1–6

be improved straightforwardly if temperature is a concern in future experiments. The sample is imaged through an objective (Mitutoyo 50X Plan Apochromat, NA: 0.55, WD: 13 mm). The objective is outside the cryostat; the image is taken through a window in the top of the cryostat and recorded on a camera (Thorlabs, Zelux). Besides the imaging path, all probe lasers are sent through the objective. The green cw laser (Cobolt MLD-06 515 nm) and green pulsed laser (NKT Onefive Katana, 532 nm, 65 ps) are combined with a 50/50 fiber beam splitter. One of the outputs is used for power calibration (PWR, Thorlabs S120C), and the other one is sent to the sample. Similarly, the red cw laser (Toptica TA-SHG Pro, 619 nm) and white laser (NKT SuperK compact) are also combined on a 50/50 fiber beam splitter. In the red laser path, there is a fiber bench (Thorlabs FBP-A-FC) with a $\lambda/2$ waveplate, $\lambda/4$, and a linear polarizer (Thorlabs FBR-AH1, FBR-AQ1, and FBR-LPVIS). The purpose of the fiber bench is to clean up the polarization and couple from PM to SM fiber. The white laser is spectrally filtered using a 600 nm long-pass and a 700 nm short-pass filter. Collection is performed using a tapered optical fiber (Thorlabs, SM600). The fiber is tapered in 40% hydrofluoric acid [60]. The fiber-to-waveguide coupling is estimated to be about 30% [11]. For the cryogenic measurements, the tapered fiber is passed through a vacuum-tight Teflon feedthrough and connected to the detection setup (Fig. 7, bottom left). Here, the collected light is split into PSB and ZPL using a dichroic beam splitter (Semrock, FF625-SDi01). The PSB light is filtered by a tunable long-pass filter (Semrock, TLP01-628). For the lifetime measurements (Fig. 3), we use off-resonant pulsed excitation. Thus, we can excite multiple SnVs within the objective focus. The ZPL path needs to spectrally filter the collected light to contain only the emission of the SnV we want to probe. Therefore, we use a combination of a 40 GHz etalon (LightMachinery), a 4 GHz etalon (LightMachinery, OP-7423-843-1), and a 620 nm bandpass (Thorlabs, FBH620-10). The 4 GHz etalon can drift on the timescale of tens of minutes. We have placed it on a rotation stage (Thorlabs, K10CR1/M) and continuously reoptimized the angle. For the reflection measurements (Appendix K), we probe the PCC with the red laser from the tapered fiber. During these measurements, we insert a beam splitter between the red laser and the tapered fiber (Fig. 7, bottom right). The beam splitter sends 20% of the probe light to the sample and collects 80% of the emission. The polarization of the probe light is controlled with a motorized fiber paddle (Thorlabs, MPC320). The collected light is sent to the usual detection setup.

APPENDIX C: CAVITY DESIGN AND DEVICE LAYOUT

The design of the symmetric photonic crystal cavity version was developed in Ref. [39]. The geometrical parameters are summarized in Table I. The defect is introduced with a functional form as in Ref. [61], where the lattice constant is adiabatically varied symmetrically on either side of the defect region following

$$a_i = a(1 - d(2y_i^3 - 3y_i^2 + 1)), \quad i = 0, \ldots, N, \tag{C1}$$

where y_i is given by

$$y_i = \begin{cases} \frac{1}{2}(2x_i)^\eta & x_i \le 0.5 \\ 1 - \frac{1}{2}(2(1-x_i))^\eta & x_i > 0.5, \end{cases} \tag{C2}$$

with $x_i = i/N$ and $i = 0$ being the center of the cavity. The other side is mirrored. Equation (C2) is a functional form that ensures the derivative of a with respect to i to be zero on the sides and in the center. In Fig. 9, we show the band structure of the unit cell and classify the modes according to

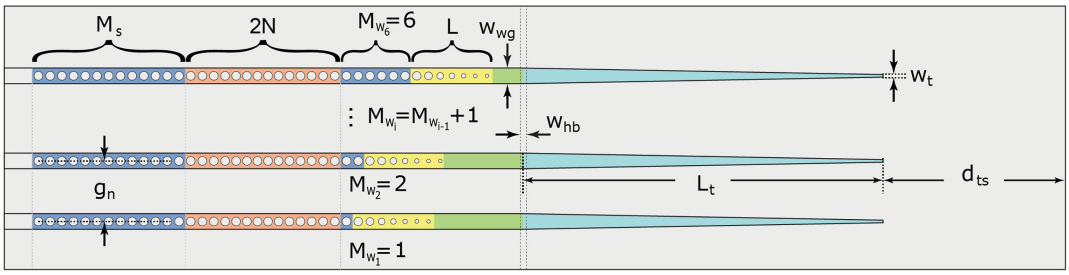

FIG. 8. Schematic illustration of free-hanging, single-sided, photonic crystal cavity design (inspired from Ref. [35]), in an array of device configurations.

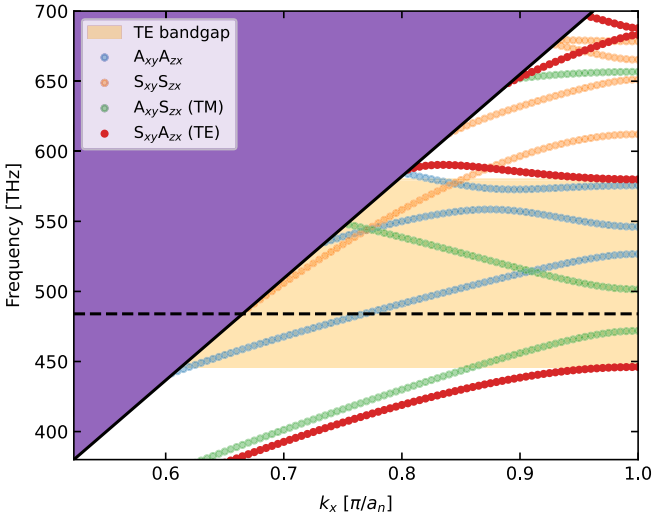

FIG. 9. Band structure of the designed cavity. We classify the modes depending on the symmetry of the tangential electric field with respect to two planes. The dashed line represents the SnV's ZPL emission frequency. Axes are defined in Fig. 11(b). An alternative notation for the mode symmetry is $E_{(o,n)} \leftrightarrow S_{xy}A_{zx}$, $E_{(e,n)} \leftrightarrow S_{xy}S_{zx}$, $M_{(e,n)} \leftrightarrow A_{xy}S_{zx}$, and $M_{(o,n)} \leftrightarrow A_{xy}A_{zx}$, with $n = 1, 2, \ldots$ the order of the mode [62].

the symmetry of the tangential electric field with respect to two planes: XY and ZX, with x parallel to the beam.

The devices are single-sided photonic crystal cavities (schematically illustrated in Fig. 8). The cavity design parameters are summarized in Table I, and the complete overview of the array of device parameters is summarized in Table II. The cavities consist of a strong mirror (over M_s mirror unit cells, blue-shaded area), a central cavity region (over 2N unit cells, red-shaded area), and a weak mirror (over M_w variable number of mirror holes, right, blue-shaded area). The cavity design is inspired from Ref. [35], where we maintain a constant value of the lattice constant a_n, equal for both the strong and weak mirrors. Effectively, in the presented design, the two mirrors have the same stop band, with the weak mirror characterized by a reflectance dependent on the number of mirror unit cells M_w. The directionality in the out-coupling from the cavity to the waveguide is realized by reducing the number of mirror unit cells. Next to the weak in-coupling mirror, the latter is adiabatically tapered to the waveguide region (green shaded, with the width w_{wg} the same as the cavity width) by appending additional L mirror unit cells (yellow shaded) with the same value of the lattice constant, a_n, as in M_s and M_w. The radius of the additional L mirror unit cells is linearly decreased from a nominal value of radius r to r_{min} by using a simple linear functional form. The value of r_{min} is chosen to be around 25 nm, which is the lowest value that can be successfully fabricated with the QIE-based fabrication process parameters in this work. Next, the waveguide width is reduced from w_{wg} to the end-taper width w_t, over L_t taper length (cyan).

TABLE II. Device design parameters.

Parameter	Symbol	Value
Tapered mirror unit cells	L	7
Coupling taper-end width	w_t	50 nm
(Optional) holding bar width	w_{hb}	200 nm
Center-to-center device gap distance	g_n	3 μm
Coupling taper length	L_t	≃8 μm to 15 μm
Taper end to substrate distance	d_{ts}	60 μm
Coupling tapered hole radius	r_{min}	25 nm

To guarantee structural stability, a trade-off in the overall length of the free-hanging device structure, is considered, sweeping the taper length L_t. The distance from the taper end to the diamond substrate, d_{ts}, is fixed to a value significantly higher than the device taper length, which provides sufficient space for optimizing the fiber position for in-contact and lensed-fiber configurations.

The array of devices are single-sided cavities with a varying number of weak mirror holes M_w (from 1 to 6), spaced by a distance g_n. This distance is chosen to guarantee uniform device thickness across the array of devices. The devices are connected to the diamond substrate on the strong mirror side. Some arrays include a holding bar of width h_{hb} so that a longer waveguide taper L_t can be fabricated. The holding bar is attached to the bulk substrate, and it supports all devices within the same array, preventing the devices with a longer taper from bending downwards and/or collapsing.

On the overall diamond substrate, we sweep the cavity device design by varying the scaling factor on the lattice constant a_n, the waveguide width w_{wg}, and circular hole radius r incrementally by $\Delta = 1\%$, with respect to the nominal values (scaling factor 100%) determined via the finite element method optical simulations in COMSOL. We vary the scaling factor from 95% to 110% with respect to nominal 100% device parameters. As a result, we obtain several arrays of devices with scaling factors that enable us to preventively compensate cavity resonance shifts from the fabrication process variability and to yield cavity devices with resonances less than or around 619 nm (SnV center emission), thus allowing for dynamic *in situ* cavity resonance tuning to the embedded SnV center emission lines.

APPENDIX D: FABRICATION PROCESS

The devices presented in this work are fabricated in two main phases: SnV creation and nanophotonic device fabrication, respectively. SnV centers are generated by ion implantation and high-temperature annealing, for which the main parameters are summarized in Table III. The sample fabrication process starts with the preimplantation surface treatment of a {001} surface-oriented electronic-grade diamond substrate (ElementSix). The sample

TABLE III. Main steps and parameters for SnV center creation. Left: Preanneal substrate preparation. Center: Sn ion implantation parameters. Right: SnV center activation.

	Preanneal substrate preparation			Sn implantation		SnV activation		
Step	Clean	Strain relief	Clean			Clean	Anneal	Clean
Parameter	HF 40% + 2x Piranha	Ar/Cl_2, O_2	Piranha	Dose [ions/cm^2]	Implant angle	Tri-acid	Vacuum anneal	Piranha + di-acid
Value	20 min + 2x 20 min	5 μm + 6 μm	30 min	3×10^{10}, 1×10^{11}	7°	4 hours 120 °C	4 hours @ 1100 °C	20 min @ 80 °C+ 4 hours @ 190 °C

substrate is first cleaned in a wet HF 40% inorganic solution at room temperature for 20 min, followed by Piranha [ratio 3∶1 of H_2SO_4 (95%): H_2O_2 (31%)] inorganic solution for 20 min at 80 °C. Next, the superficial etching of around 5 μm via the inductively coupled-plasma reactive-ion-etching (ICP-RIE) Ar/Cl_2 plasma chemistry recipe follows, in order to remove the residual polishing-induced strain from the surface of the substrate. An additional ICP-RIE O_2 chemistry plasma etch of around 6 μm is performed in order to remove residual chlorine contamination from the previous etching step [39]. The sample is then inorganically cleaned in a Piranha solution (20 min at 80 °C) and implanted with ^{120}Sn ions. The implantation is performed in two steps. First, half of the sample is covered by a 500 μm thick piece of silicon, and the sample is implanted with a dose of 7×10^{10} ions/cm^2. Then, the silicon cover is removed, and the sample is implanted again with a dose of 3×10^{10} ions/cm^2. This method results in two regions with implantation doses of 3×10^{10} and 1×10^{11} ions/cm^2, respectively. All cavities investigated are in the high implantation dose region. We use an implantation energy of 350 keV at an angle of 7°. Prior to the activation of the SnV centers by high-temperature, low-pressure annealing (1100 °C with the surface-protected annealing method [40]), a triacid cleaning [ratio 1∶1∶1 of $HClO_4$(70%): HNO_3(70%): H_2SO_4(> 99%), at 120 °C] is performed for 4 hours in order to remove any residual organic contamination, whereas in postannealing, the sample undergoes a 30-min Piranha cleaning at 80 °C and 4-hour di-acid cleaning [ratio 1∶1 of $HClO_4$(70%): H_2SO_4(> 99%), at 190 °C] in order to remove any superficial graphite thin film layers (on noncovered edges of the diamond substrate), as well as to guarantee an oxygen surface termination for the graphite-free overall substrate surface. To assess the successful activation of the SnV centers, the sample is characterized (prior to the nanofabrication of the suspended structures) at 5 K in a closed-cycle cryostat to identify the activated SnV centers (employing PL and PLE measurement sequences).

The nanofabrication of PCC structures (developed in Ref. [40]) follows the crystal-dependent QIE undercut-based fabrication process developed in Refs. [22,30,36–39]. A schematic of this process is shown in Refs. [11,40].

Specifically, we start with an extensive inorganic clean for 20 min in HF (40%) at room temperature, followed by a double Piranha [ratio 3∶1 of H_2SO_4 (95%): H_2O_2 (31%)] inorganic solution for 20 min at 80 °C each.

Next, we perform deposition, via inductively coupled plasma-chemical-vapor deposition (ICPCVD), and patterning of a hard mask material, consisting of a thin film layer of around 81 nm Si_xN_y. The PCC design is longitudinally aligned with the $\langle 110 \rangle$ diamond crystallographic orientation and exposed via e-beam lithography of around 220 nm of AR-P-6200.09 positive tone resist. To avoid charging effects of the diamond substrate during the e-beam exposure, the surface of the e-beam resist is coated with about 40 nm of Electra 92 (AR-PC 5090) conductive polymer. Next, after e-beam exposure, it is removed by immersing the sample in 60 s gentle stirring in H_2O and N_2 blow-dry (to dissolve Electra 92 and fully dry the residual H_2O). The resist is then developed in 60 s pentyl acetate, 5 s ortho-xylene, and 60 s isopropyl alcohol (IPA). We then proceed with the transfer pattern into the Si_xN_y hard mask material by means of ICP-RIE etch in a CHF_3/O_2 based plasma chemistry. Next, the complete removal of residual e-beam resist in a twofold wet step follows: We first proceed with a coarse resist removal in a PRS 3000 positive resist stripper solution, followed by fine removal of resist residues in an extensive double Piranha inorganic clean. Such considerable inorganic cleaning is employed to prevent micromasking within the next dry etch steps that can potentially be caused by organic residues on the sample.

The pattern from the Si_xN_y hard mask material is transferred in the diamond substrate by top-down etching in a dry ICP-RIE O_2 anisotropic etch for an extent of around 2.5 times the designed thickness of the devices. It is crucial to note that the O_2 dry etch heavily affects the aspect ratio of the patterned Si_xN_y hard mask: We observe the etch rate of Si_xN_y to be higher at the edges of the patterned structures compared to the determined etch rate of Si_xN_y on flat area test samples, leading to enhanced erosion of the Si_xN_y at the edges of the nanostructures. This feature yields rounded vertical sidewalls with a few nanometers of hard mask material at the diamond-to-Si_xN_y interface [39], leading to weak points across the top surface of the hard mask that can compromise the integrity of the hard mask in

the downstream QIE-based process fabrication steps. We circumvent this challenge by carefully tuning the trade-off between sufficient anisotropic diamond etch and Si_xN_y mask integrity, such that the latter withstands the following ICP-RIE dry etch steps foreseen by the overall QIE-based fabrication process.

Next, we perform a conformal atomic layer deposition (ALD) of about 25 nm of AlO_x for hard mask coverage of devices vertical sidewalls. The horizontal coverage of AlO_x is then fully removed by ICP-RIE etch in a BCl_3/Cl_2 plasma chemistry. This process opens access to the diamond substrate: We directly follow with sequential QIE undercut and upward etch steps, interleaved by SEM monitoring. The full release and upward quasi-isotropic total etch time is considerably shorter (85 min) when compared to the 65 °C QIE undercut recipe, which is demonstrated to be suitable for a complete undercut of nanophotonic waveguides [11]. Finally, the hard mask materials are removed in extensive inorganic treatment for 20 min in HF (40%) at room temperature.

The overall qualitative characterization of the fabrication steps presented in this work has been executed on a scanning electron microscope Hitachi SEM Regulus system. The ICPCVD deposition rates and ICP-RIE etch rates have been precharacterized on additional test samples, in parallel to the fabrication of the diamond sample employed in this work following the same fabrication methods and parameters. Such etch tests have been conducted by employing silicon substrate samples, with the thin films of interest deposited in parallel to the diamond substrate. Optical parameters and thickness of the employed materials have been determined via a spectroscopic ellipsometry method on a Woollam M-2000 (XI-210) tool. The QIE rate has been characterized by employing supplementary diamond test samples (fabrication parallel to the sample in this work) and analyzed via SEM inspection. The cross section of the obtained diamond devices has been determined from a combination of high-magnification SEM (Hitachi SEM Regulus) inspection and atomic force microscopy (Bruker FastScan AFM) topographic analysis.

APPENDIX E: DEVICE GEOMETRY CHARACTERIZATION

The QIE-based fabrication process unavoidably introduces inaccuracy in the fabricated device geometry, deviating from the simulated rectangular unit cell. This inaccuracy prevalently affects the hole radius r, the device width w_{wg}, and the device cross section (as shown in Fig. 10), inherently reducing the quality factor and shifting the cavity resonance with respect to the original design. Here, we present the quantitative analysis on a typical consistent geometry bias and transversal cross section by combining SEM inspection and AFM topography analysis. The device geometry analysis is performed on two twin diamond samples (SEM geometry analysis on Sample 2, AFM topography analysis on Sample 3), fabricated within the same fabrication run and the same fabrication process parameters as the sample used in this work (Sample 1).

Transfer pattern accuracy (a_n, r, and w_{wg}) yields differences on the order of a few nanometers (not quantifiable via SEM analysis), whereas device thickness variability is about 10 nm between the analyzed samples (Sample 2 and Sample 3 have a device thickness of about 10 nm lower than Sample 1). The transversal device cross section estimated in the following section (namely, vertical sidewall angle deviation and bottom facet topography) is representative of the three fabricated diamond substrates.

High-magnification SEM analysis of Sample 2 [Fig. 10(b), 0° tilt angle view, pixel size around 0.52 nm] enables inspection of the fabricated device top facet, allowing for accurate estimation of the lattice constant a_n, hole radius r, and device width w_{wg}. In this example, the analysis is carried out on a PCC device with scaling of 95% ($a_n = 0.95 \times 206$ nm $= 195.7$ nm, $r = 0.95 \times 71$ nm $= 67.45$ nm, $w_{wg} = 0.95 \times 275$ nm $= 261.25$ nm), which is the smallest device dimension we pattern in our typical parameter scaling factor sweep.

Overlaying the computer-aided design (CAD) device geometry [Fig. 10(b), dashed green] on the SEM pictogram of the corresponding fabricated device (at scaling factor 95%) (pixel size 0.53 nm), no significant deviation from the optimal a_n can be observed, confirming a high accuracy of a_n in the transfer pattern. When comparing the circular hole diameter and device width on the top facet (dashed orange) with the design parameters (r and w_{wg}), an r systematic bias of around 4 nm (radius larger than design) and a w_{wg} systematic bias of around 20 nm (width smaller than design) can be identified.

Next, high-magnification top-down SEM inspection allows for an estimation of the vertical sidewall angle. In other words, in the case of a design sidewall angle of 90°, the top facet contour [Fig. 10(b), dashed orange] of etched devices should perfectly align with the bottom facet contour (dashed yellow). By measuring the horizontal extent between the top facet contours and bottom facet contours, we identify, on average, a distance of around 10 nm, indicating that the sidewall angle is less than or around 90°. When measuring the same quantity on a scaling factor 100% ($a_n = 206$ nm, $r = 71$ nm, $w_{wg} = 275$ nm) PCC device, we find similar values, within the SEM pixel-size resolution error, thus independent of the absolute parameter values, given a certain device scaling factor. A measurement of the (same scaling factor of 95%) device thickness from SEM inspection [45° tilt angle view, pixel size 1.98 nm, Fig. 10(d)] yields a vertical extent from the top facet to the bottom facet of around 188 nm. Assuming the bottom facet of the device is characterized by a flat planar surface, the estimated sidewall angle deviation from the design of around 90° is around 3°.

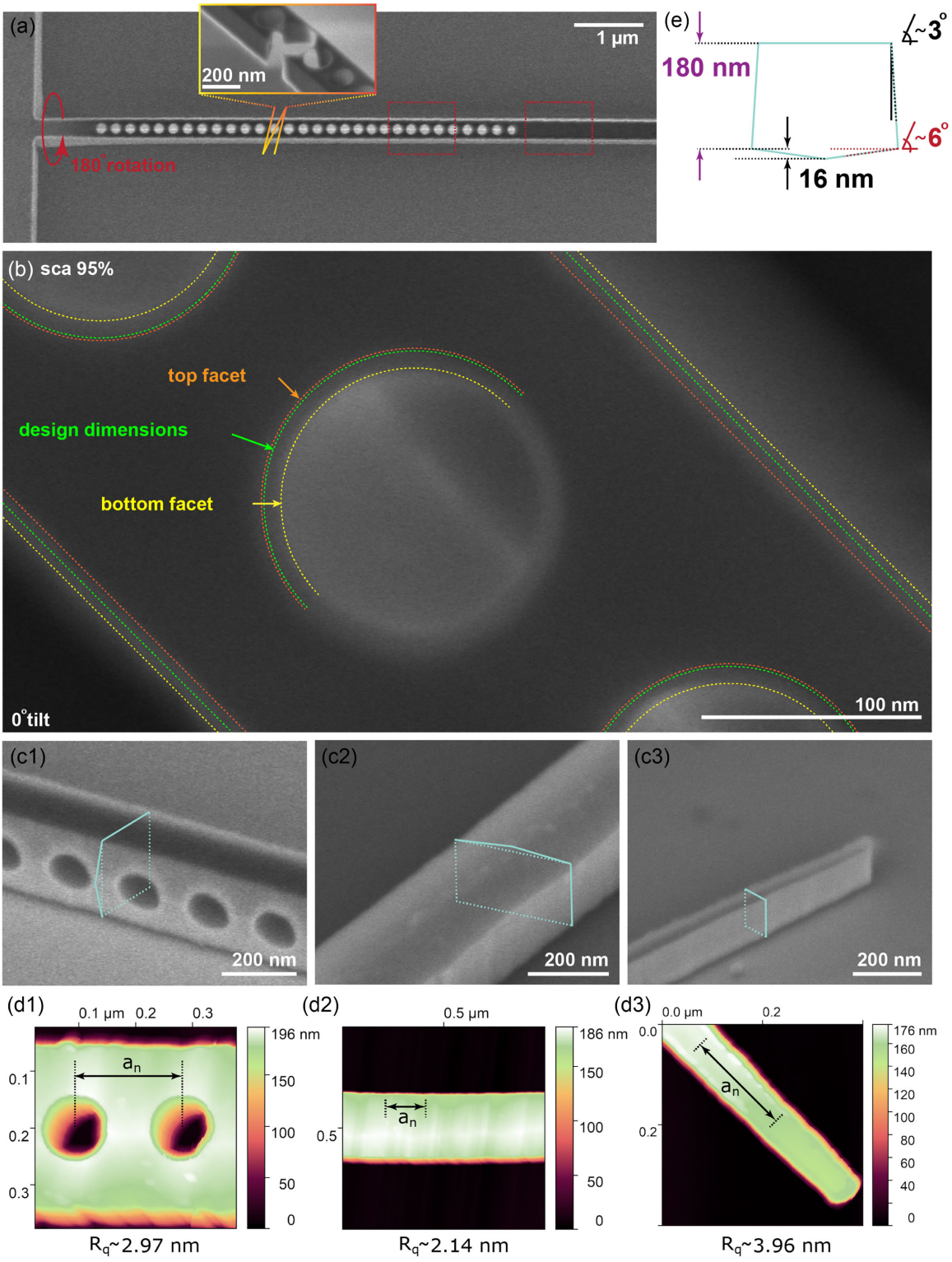

FIG. 10. SEM and AFM device geometry characterization on twin diamond samples (Sample 2 and Sample 3), representative examples of QIE-based fabrication process performance. (a) Typical diamond photonic crystal cavity. (b) High-magnification SEM of a PCC transfer pattern on Sample 2. (c) SEM of the device backside of (c.1) cavity region, (c.2) waveguide region, and (c.3) taper-end region. (d) AFM topography analysis (Sample 3) of device bottom facet: cross section and surface roughness R_q (evaluated over $a_n = 196$ nm) of (d.1) cavity region, V-shaped triangular cross section, and $R_q = 2.97$ nm, (d.2) waveguide region, V-shaped triangular cross section, and $R_q = 2.14$ nm, (d.3) taper-end region, rectangular cross section, and $R_q = 3.96$ nm. (e) Estimated full cross section of the device in the cavity region from a combination of AFM topography and top-down high-magnification SEM.

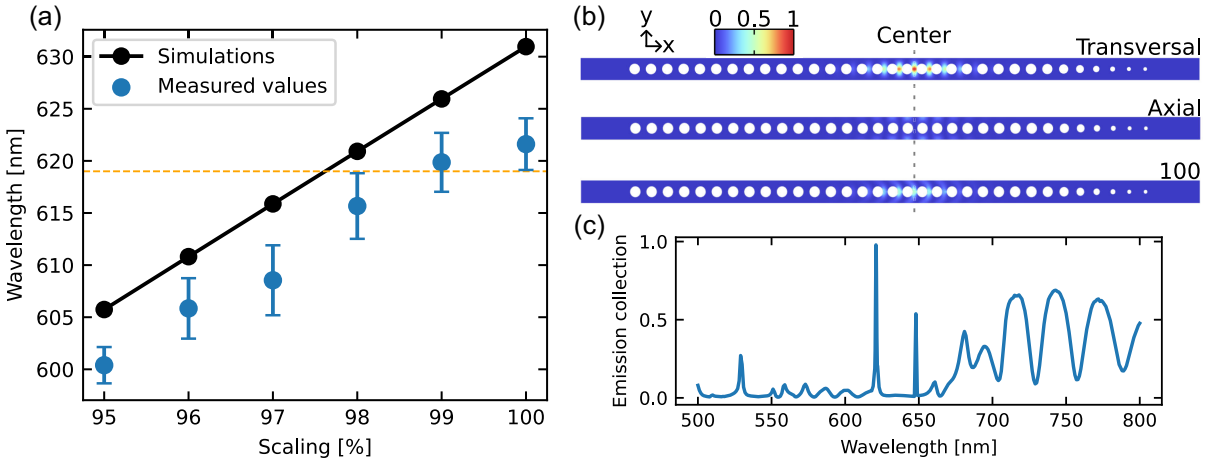

FIG. 11. Cavity properties. (a) Resonance wavelengths as a function of the scaling parameter extracted from simulations (black) and measured statistical averages (blue). The orange dashed line lies at 619 nm, the ZPL of the SnV center. The error bars indicate $\pm 1\sigma$. (b) Cooperativity color map as a function of the emitter's position and the three dipole orientations. We normalize to the maximum cooperativity, found at the center of the transversal case. (c) Fraction of the emission collected in the waveguide from a y-polarized dipole centered in the cavity as a function of the emission wavelength. The two central peaks correspond to the fundamental and first-order cavity modes.

In the typical array-of-devices layout [Fig. 10(a)], free-hanging devices are attached to the bulk diamond substrate from the end side of the strong mirror region of the device. On diamond Sample 3, a device-breaking mechanism is present (shown in inset). By SEM inspecting the broken PCC structures, we are able to identify the parent array of devices. For devices repositioned to expose the bottom facet, qualitative SEM inspection of the cavity region and waveguide region [Figs. 10(c.1) and 10(c.2), respectively, on three separate broken devices from different parent arrays of devices across the sample] allows one to SEM resolve a triangular cross section and a rectangular cross section in the taper-end region [Fig. 10(c.3)]. At the same time, SEM-resolved surface roughness can be identified; thus, taking into account the pixel size [Figs. 10(c.1), 3.17 nm; 10(c.2), 1.98 nm; and 10(c.3), 1.44 nm pixel size, respectively) in the pictograms shown, we suspect the surface roughness of the bottom facet to be of similar order of magnitude.

Next, the AFM topography scan on Sample 3 (representative of typical fabrication imperfections) of a PCC device (scaling factor 98%) exposing the topside facet enables a quantitative evaluation of the circular hole diameter and waveguide width. This process allows us to quantify the discrepancy between the top-facet and design parameter values from topographic measurements. A consecutive AFM topography scan of a PCC device (scaling 97%) exposing the bottom facet enables both a quantitative evaluation of the bottom topography cross section and a surface roughness evaluation, as shown in Figs. 10(d.1)–10(d.3), respectively.

By comparing the top-side facet and the bottom-side facet evaluated values of the hole radius r and waveguide width w_{wg}, the AFM analysis confirms the accuracy of the SEM analysis presented above, here measuring a device's bottom facet w_{wg} extent around 20 nm higher and an r extent about 10 nm lower when comparing to the same parameters measured on the device's top facet. Next, the topography maps of the cavity region and waveguide region show a triangular V-shape bottom facet, with a height of around 16 nm, whereas the topography map of the taper end displays a rectangular cross section.

Combining the evaluated experimentally measured device parameters allows us to infer the PCC device cavity and waveguide region cross section, where we estimate the vertical sidewall angle to be around 3° and the bottom facet to be V-shaped with an angle around 6°, as schematically illustrated in Fig. 10(e). The total thickness difference between the cavity and waveguide regions is around 10 nm in the specifically evaluated 97% device scaling factor presented here. The observed device geometry reflects the nature of the aspect-ratio QIE undercut dependency, for

TABLE IV. Devices statistics.

Parameter	Sample 1	Sample 2
Investigated	232	254
With resonance	200	216
Visually broken	22	25
No resonance	10	13
Q measured	163	164
Not in reflection	27	7
Spectrometer range	7	0
Spectrometer resolution	0	39
Fit error > 20%	3	8

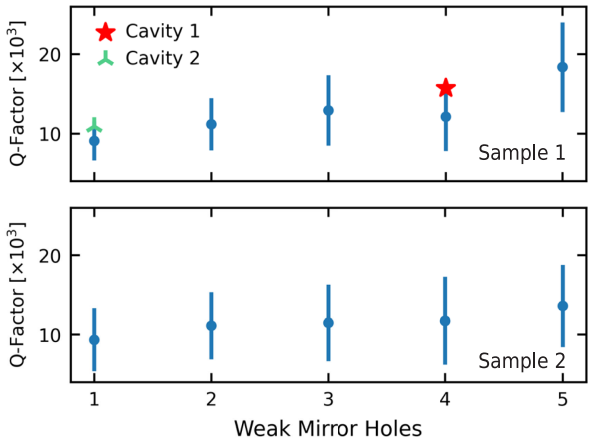

FIG. 12. Quality factors as a function of weak mirror holes for Sample 1 (top panel) and Sample 2 (bottom panel). The error bars indicate $\pm 1\sigma$.

which the complete upward etch flattening of narrow devices (i.e., design taper-end width of $w_t = 50$ nm) takes place earlier in the etch process, when compared to wider devices (i.e., design cavity and waveguide region width of $w_t = 275$ nm).

APPENDIX F: DEVICE STATISTICS

The reported quality factor statistics exclude several devices from the investigated subset on each fabricated diamond sample. For Sample 1, we report a total of 163 quality factors, excluding devices where the fundamental cavity mode falls outside the range of our spectrometer (7) or where we observe a cavity resonance but the measurement contrast in reflection is too low to attribute a quality factor (27) to. For these cavities, one can measure a resonance when the fiber is placed on top of the cavity. However, this influences the quality factor, so we do not attribute a value for Q.

For Sample 2, there are (39) cavities where the first higher order mode can be observed and the fundamental mode should fall within the spectrometer range (the distance between the fundamental mode and the first higher order mode is around 30 nm). However, no fundamental mode is observed. We attribute this finding to the limited spectrometer resolution.

For both samples, there is a small effect where cavities with more weak-mirror holes have a higher average quality factor, as shown in Fig. 12. However, this effect is generally smaller than the variance of quality factors among devices with the same number of weak mirror holes.

APPENDIX G: CAVITY SIMULATIONS

The fabrication process introduces systematic imperfections in the geometry, namely, deviations in the width of the nanobeam, sidewall angles, and nonflat bottom surfaces. Therefore, the cavity design with the nominal parameters presented in the previous section is not expected to fully reproduce the measured characteristics of the cavities. These imperfections are compensated by fabricating devices with a smaller thickness (from 230 nm to 188 nm) and introducing a scaling parameter. The latter is a scaling factor that is applied to all geometrical parameters, except for thickness, and is swept on the fabricated sample.

After measuring the device cross section via SEM and AFM, we incorporate it into our FEM simulations with COMSOL Multiphysics [63]. We find a disagreement of around 6 nm between our simulations and the average cavity resonances measured at room temperature [see Fig. 11(a)].

Based on the simulated electric fields, we plot the cooperativity as a function of the emitter position and dipole orientation in Fig. 11(b). These figures illustrate the importance of deterministic positioning of the color centers to achieve the maximum possible cooperativities. For the latter, we use the following definition [15,31]:

$$C_{\text{bulk}} := \frac{\tau_{\text{bulk}}}{\tau(\Delta = 0)} = \frac{3}{4\pi^2} \frac{Q}{\frac{V}{(\lambda/n)^3}} |\hat{d}_i \cdot \hat{E}(\vec{x})|^2 \cdot u^2(\vec{x}) \cdot \beta_0, \tag{G1}$$

where τ_{bulk} is the lifetime of a SnV center in bulk diamond, $\tau(\Delta = 0)$ is the lifetime of the SnV when in resonance with the cavity, Q is the quality factor of the cavity mode, $V := \{[\int \epsilon(\vec{x})|E|^2 dV]/[\max\{\epsilon(\vec{x})|\vec{E}(\vec{x})|^2\}]\}$ is the mode volume, λ is the vacuum wavelength of the emitter and cavity at resonance, n is the refractive index of diamond, $\hat{E}(\vec{x})$ is the unit vector for the electric field at the emitter's location $\vec{x}$, $u^2(\vec{x}) := \{[\epsilon(\vec{x})|\vec{E}(\vec{x})|^2]/[\max\{\epsilon(\vec{x})|\vec{E}(\vec{x})|^2\}]\}$, and β_0 is the fraction of decay from the excited state into the line resonant with the cavity.

The orientation of the electric dipole of the emitter is along the $\langle 111 \rangle$ crystallographic axis of diamond and is denoted by $\hat{d}_i$. We consider three dipole orientations $i \in \{\text{transversal}, \text{axial}, \langle 100 \rangle\}$, where

$$\hat{d}_{\text{transversal}} = \frac{1}{\sqrt{3}}(0, \sqrt{2}, 1), \tag{G2}$$

$$\hat{d}_{\text{axial}} = \frac{1}{\sqrt{3}}(\sqrt{2}, 0, 1), \tag{G3}$$

$$\hat{d}_{\langle 100 \rangle} = \frac{1}{\sqrt{3}}(1, 1, 1), \tag{G4}$$

which are defined with respect to the coordinate axes in Fig. 11(b). The devices in the main text are fabricated along the $\langle 110 \rangle$ crystallographic axis of diamond, so only the transversal and axial orientations are possible. The remaining dipole orientation considered would correspond to a device fabricated along the $\langle 100 \rangle$ crystallographic axis.

Note that this definition of cooperativity compares the rate of emission into the cavity at resonance with the spontaneous decay rate of the emitter in bulk diamond. However, in our case, the emitter is in a nanophotonic structure. A more accurate definition of cooperativity that is found experimentally would be $C \coloneqq \{[\gamma'(\Delta = 0) - \gamma'(\Delta \to \infty)]/[\gamma'(\Delta \to \infty)]\}$, which simply compares the decay rates of the emitter between the off- and on-resonance cases. The latter is the cooperativity reported in the main text. The lifetime of an emitter in a nanophotonic structure is expected to be larger the closer it is to a vacuum interface [42]. Therefore, the definition of Eq. (G1) is a lower bound for the attainable cooperativities.

Additionally, we simulate a y-polarized electric dipole in the center of the cavity and compute the fraction of power that exits through the coupling waveguide mode. In Fig. 11(c), we plot this transmission as a function of the dipole's frequency. We observe a high transmission when the dipole is on resonance with the two cavity modes but also at longer wavelengths. Therefore, both the ZPL and part of the PSB of the emitters can be collected through the waveguide. More specifically, the total emission in the PSB range (625 nm to 700 nm [42]) is around 44% that of the same emitter in a waveguide.

We now investigate the directional decay rates of the cavity. The total cavity decay rate $\kappa = \omega/Q$ can be decomposed into two decay rates $\kappa = \kappa_e + \kappa_i$, where κ_e is the decay rate into the waveguide and κ_i is the intrinsic decay rate, which includes all other decay channels. The simulations naturally provide the total decay rate κ from the solution to an eigenvalue equation. We then compute the ratio between the power exiting through the waveguide and the power exiting through the entire domain. From the equality $P_{\text{waveguide}}/P_{\text{domain}} = \kappa_e/\kappa$, we can extract κ_e.

Starting from a device with a simulated $Q \sim 4 \times 10^6$, Fig. 13(c) shows that the coupling factor into the waveguide κ_e/κ goes to around 1 (blue curve) as the number of unit cells in the weak mirror region is lowered. However, the second device that we measure, which has one unit cell in the weak mirror region, only achieves a coupling factor $\kappa_e/\kappa = 0.31$ (see Appendix K). The discrepancy between the simulated and measured values arises because the intrinsic decay rate κ_i of the fabricated devices is much faster ($Q \sim 10^4$, see Table V) due to additional scattering losses, such as bottom surface roughness, whereas the decay rate into the waveguide κ_e remains roughly equal, thereby lowering the coupling efficiency $\kappa_e/(\kappa_e + \kappa_i)$.

To demonstrate that κ_e is roughly independent of these scattering losses, we artificially introduce absorption into the cavity by adding an imaginary part to the refractive index of the diamond that makes up the cavity. The formula to extract κ_e becomes $P_{\text{waveguide}}/(P_{\text{domain}} + P_{\text{absorption}}) = \kappa_e/\kappa$. In Fig. 13(a), we see that κ_e remains the same (orange curve), whereas κ increases as expected [see Fig. 13(b)]. In this case, we obtain a coupling factor $\kappa_e/\kappa \sim 0.06$ for a weak mirror of one unit cell, which underestimates the measured coupling factor.

The number of unit cells in the taper region is seven by design. However, most devices on the sample only have two; the rest did not open. We remove the latter from the simulation and find that the decay rate into the waveguide increases (green curves), resulting in a coupling factor of $\kappa_e/\kappa \sim 0.28$ for a weak mirror of one unit cell, which is probably because the taper region also acts like a mirror and reducing the number of unit cells further weakens the mirror.

The simulated device with absorption and two unit cells in the taper region has a $Q \sim 10^4$ at one unit cell in the weak mirror region, similar to Device 2 (see Table V). We further find a simulated $\kappa_e \sim 13$ GHz that is in good order-of-magnitude agreement with the measured value $\kappa_e \sim 8$ GHz. Thus, in order to fabricate overcoupled devices, the

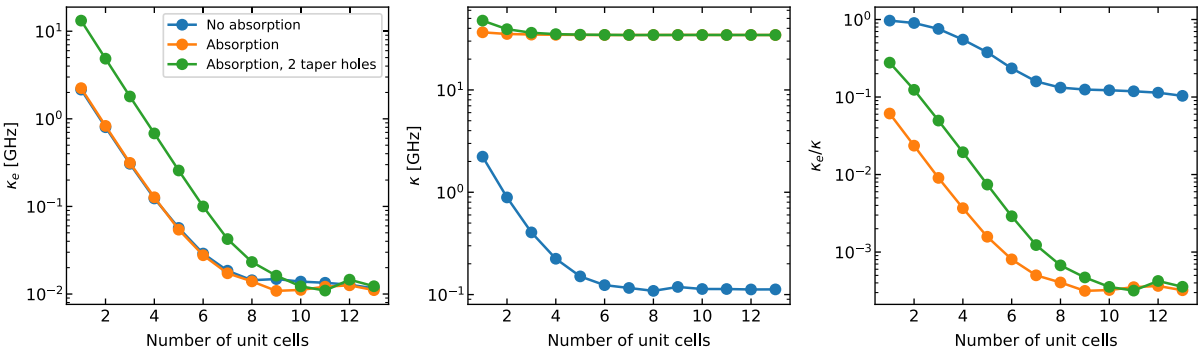

FIG. 13. Directional decay rates and waveguide coupling efficiencies. (a) Waveguide decay rates κ_e, (b) total decay rates κ, and (c) waveguide coupling efficiencies κ_e/κ as a function of the number of unit cells in the weak mirror region. The three curves correspond to a cavity without absorption and all the unit cells in the taper region (blue), a cavity with absorption and all the unit cells in the taper region (orange), and a cavity with absorption and only two unit cells in the taper region (green). We used an imaginary component for the refractive index of 10^{-4}.

TABLE V. C-QED parameters.

Parameter	Symbol	Device 1	Device 2	Source
Cavity parameters				
Cavity decay rate	κ	$2\pi \times (19.0 \pm 0.3)$ GHz	$2\pi \times (47.5 \pm 2.1)$ GHz	Figs. 4(c) and 18(a)
External decay rate	κ_e	$2\pi \times (4.1 \pm 0.1)$ GHz	$2\pi \times (14.5 \pm 0.6)$ GHz	Fig. 17
Internal decay rate	κ_i	$2\pi \times (14.9 \pm 0.2)$ GHz	$2\pi \times (33.0 \pm 1.0)$ GHz	Fig. 17
External coupling	κ_e/κ	0.214 ± 0.002	0.306 ± 0.002	Fig. 17
Unit-cell weak mirror	M_w	4	1	Design
Quality factor	Q	$(25.40 \pm 0.37) \times 10^3$	$(10.20 \pm 0.44) \times 10^3$	ω/κ
Mode volume	Vn^3/λ^3	0.45		FEM simulations
Purcell factor	F_P	$(4.200 \pm 0.061) \times 10^3$	$(1.680 \pm 0.073) \times 10^3$	$\frac{3}{4\pi^2}\frac{Q}{Vn^3/\lambda^3}$
Emitter parameters				
Lifetime	τ_0	(6.7 ± 0.3) ns	(7.26 ± 0.4) ns	Figs. 3(c) and 18(e)
Natural linewidth	γ_0	$2\pi \times (23.7 \pm 1.1)$ MHz	$2\pi \times (21.9 \pm 1.2)$ MHz	Figs. 3(c) and 18(e)
Linewidth	γ	$2\pi \times (97.5 \pm 4.4)$ MHz	$2\pi \times (53.7 \pm 1.1)$ MHz	Fig. 4(d) and off-resonant line scans
Quantum efficiency	η_Q	0.8		[41]
Debye-Waller factor	η_{DW}	0.57		[42]
Branching ratio	η_{BR}	0.8		[30]
Beta zero	β_0	0.37		$\eta_Q\eta_{DW}\eta_{BR}$
Cavity-emitter parameters				
Cooperativity	C	20.3 ± 1.1	3.5 ± 0.2	Figs. 3(c) and 18(e)
Coherent cooperativity	C_{coh}	8.3 ± 1.2	1.6 ± 0.2	Figs. 4(d) and 18(c)
Cavity-emitter coupling	g	$2\pi \times (1.94 \pm 0.08)$ GHz	$2\pi \times (0.99 \pm 0.07)$ GHz	$\sqrt{C_{coh}\kappa\gamma/4}$
Beta factor	β	0.953 ± 0.003	0.780 ± 0.002	$\frac{C}{C+1}$
Beta external	β_e	0.204 ± 0.002	0.239 ± 0.002	$\frac{\kappa_e}{\kappa}\frac{C}{C+1}$

designed κ_e should be greater than the intrinsic decay rate κ_i the fabricated devices are expected to have.

APPENDIX H: GAS TUNING

We deposit nitrogen gas onto the PCC to tune its resonance. This technique, originally reported by Mosor *et al.* [32], has been widely used [33,64–67]. The deposited nitrogen has a refractive index greater than 1 and modifies the evanescent field of the cavity. Intuitively, the PCC with deposited gas has a larger lattice constant and is thus resonant for larger wavelengths. The nitrogen (99.999% purity) flow is controlled by a leak valve (Nenion, UHV-Leakvalve ND 3). It is guided by a 1/16-inch inner-diameter stainless-steel tube assembly (Quantum Design, MI-4100-1184) directly onto the diamond sample [Fig. 14(a)]. The flow rate is set to around 1×10^{-9} mbar L/s, which results in a tuning rate of about 0.2 nm/ min [Fig. 14(b)]. After closing the valve, the resonance continues to tune for a short time, presumably due to a trace amount of gaseous nitrogen that continues to deposit. To tune the cavity backwards, we shine the green laser onto the defect region [Fig. 14(c)], which allows a precise tuning of the cavity resonance.

APPENDIX I: FITTING THE EMITTER LIFETIME

The fastest decay measured for emitter 1 is on the order of the APD jitter (400 ps). Here, we check whether the APD instrument response significantly distorts the measured decay rate. Figure 15(a) shows the calculated count rates for a pure exponential (dashed lines) and the convolution of that exponential with the measured IRF. Figure 15(b) shows the instantaneous decay constant for the curves in Fig. 15(a). The convolved signal initially shows a slower decay compared to the pure exponential, and for later times, it converges. For decays faster than a certain threshold (here, $\tau = 0.1$ ns and $\tau = 0.2$ ns), the converged value differs from the decay constant of the pure exponential. Figure 15(c) shows this threshold explicitly: Decays faster than 0.24 ns cannot be measured with this instrument. The fastest measured decay is above the instrument limit. However, we also need to check that enough of the distorted signal is excluded from the fit, which we do by shifting the start of the fit window to later times until the measured decay constant has converged, as shown in Fig. 15(d).

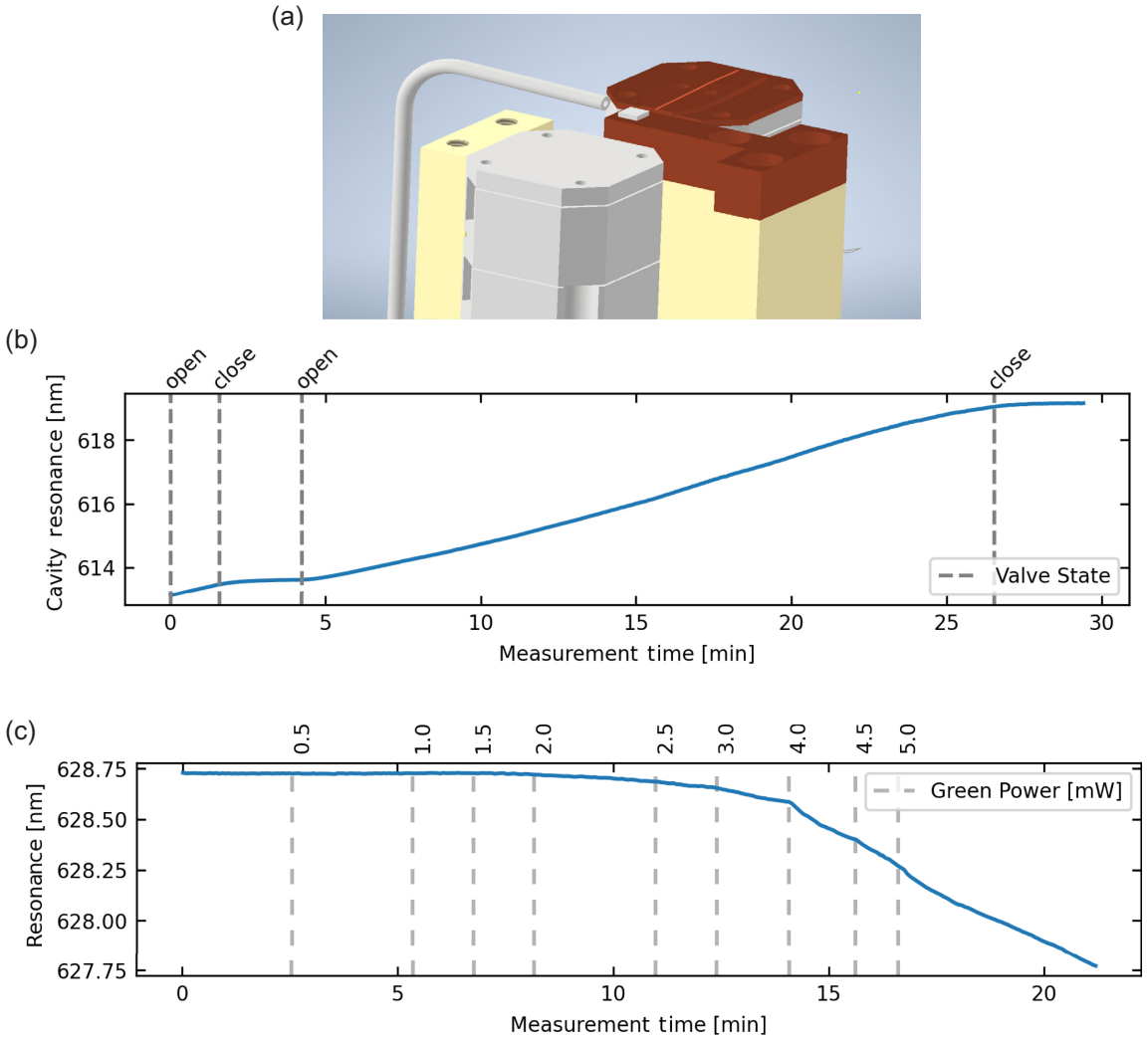

FIG. 14. Gas tuning. (a) Rendering of the inside of the cryostat. The diamond sample is glued on a copper cold finger with silver paste. A sN_2 gas line is pointed at the sample. The fiber is stuck to a machined copper holder with tape and can be moved with a piezo positioner. The second set of positioners is not used in this work. (b) PCC tuned forward by opening the leak valve (flow rate $\sim 1 \times 10^{-9}$ mbar L/s). (c) PCC tuned backward by shining a green laser onto the PCC. The speed of tuning can be adjusted by the laser power.

APPENDIX J: C-QED MODELING

At our sample temperature and in the absence of a magnetic field, we can treat the SnV center as a two-level emitter coupled to a single-mode cavity. The system's dynamics is governed by the Jaynes-Cummings Hamiltonian

$$H_{\mathrm{JC}} = \frac{\hbar}{2}\Delta_a \sigma_z + \hbar\Delta_c a^\dagger a + \hbar g(a\sigma_{\mathrm{ge}}^\dagger + a^\dagger \sigma_{\mathrm{ge}}), \qquad \text{(J1)}$$

which is given in a frame rotating with the incident laser's frequency ω. Here, $\sigma_{\mathrm{ge}} = |g\rangle\langle e|$, $\sigma_z = |e\rangle\langle e| - |g\rangle\langle g|$, and a is the cavity mode annihilation operator. The detunings are defined as $\Delta_a = \omega_a - \omega$, $\Delta_c = \omega_c - \omega$, with ω_a, ω_c the frequencies of the emitter and cavity, respectively. The cavity-emitter coupling is denoted by g. In order to remain consistent with the existing literature, in this appendix, we define Δ_a and Δ_c with an opposite sign compared to the main text. The measured observables (namely, reflected and transmitted intensities) do not vary under the simultaneous sign change.

Both the cavity and the emitter interact with bosonic baths. These bosonic baths describe the spontaneous emission of the emitter with a rate γ_0, and the different decay channels of the cavity $\kappa = \kappa_e + \kappa_i$, with κ the total decay rate, κ_e the rate into the port through which the cavity is excited, and κ_i the rate into the remaining loss channels.

The quantum Langevin equations describe the evolution of system operators in the interaction frame and are given by [68,69]

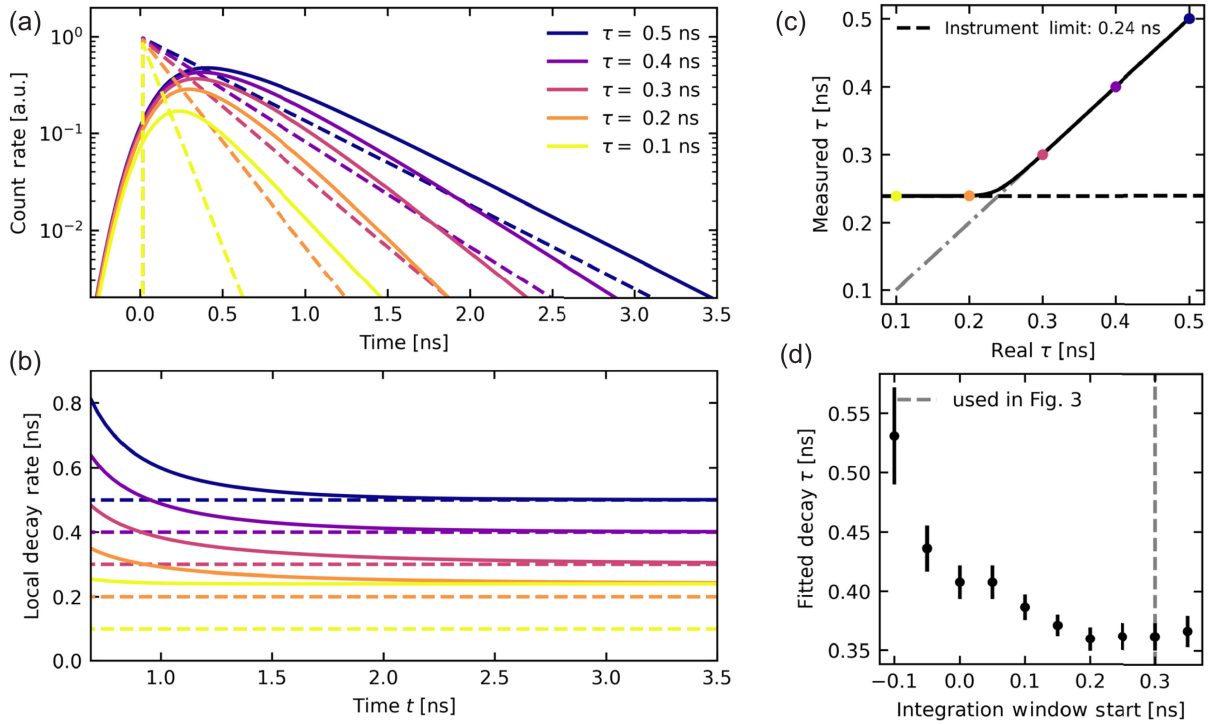

FIG. 15. Effect of the APD instrument response on the measured lifetime. (a) Perfect exponential decay (dashed lines) and the convolution with the measured IRF (solid lines) for varying decay constants τ. (b) Instantaneous decay rates for the perfect signal (dashed lines) and the convolved signal (solid lines). For $\tau = 0.1$ ns and $\tau = 0.2$ ns, the decay rates of the perfect signal and the convolved signal are asymptotically different. (c) Asymptotic decay rate of the convolved signal. Any decay rate faster than 0.24 ns cannot be measured with this instrument. (d) Convergence test to check whether the measured decay rate has converged. For the fastest decay in Fig. 3, the start of the integration window (fit window) is shifted to later times until the measured decay rate has converged. The error bars indicate $\pm 1\sigma$ uncertainty in the fit.

$$\dot{a}(t) = -i[\Delta_c a(t) + g\sigma_{\mathrm{ge}}(t)] - \frac{\kappa}{2}a(t) - [\sqrt{\kappa_e}a_{\mathrm{in}}(t) + \sqrt{\kappa_i}\xi_l(t)], \tag{J2a}$$

$$\dot{\sigma}_{\mathrm{ge}}(t) = -i[\Delta_a\sigma_{\mathrm{ge}}(t) - g\sigma_z(t)a(t)] - \frac{\gamma_0}{2}\sigma_{\mathrm{ge}}(t) + \sqrt{\gamma_0}\sigma_z(t)\xi_\gamma(t), \tag{J2b}$$

$$\dot{\sigma}_z(t) = -2ig[\sigma_{\mathrm{ge}}^\dagger(t)a(t) - a^\dagger(t)\sigma_{\mathrm{ge}}(t)] - 2\gamma_0\sigma_{\mathrm{ge}}^\dagger(t)\sigma_{\mathrm{ge}}(t) - 2\sqrt{\gamma_0}[\xi_\gamma^\dagger(t)\sigma_{\mathrm{ge}}(t) + \sigma_{\mathrm{ge}}^\dagger(t)\xi_\gamma(t)], \tag{J2c}$$

$$a_{\mathrm{out}}(t) = a_{\mathrm{in}}(t) + \sqrt{\kappa_e}a(t), \tag{J2d}$$

$$b_{\mathrm{out}}(t) = \sqrt{\kappa_i}a(t), \tag{J2e}$$

$$s_{\mathrm{out}}(t) = \sqrt{\gamma_0}\sigma_{\mathrm{ge}}(t). \tag{J2f}$$

Here, $a_{\mathrm{in}}(t)$ and $a_{\mathrm{out}}(t)$ are the input-output field operators that represent the coupling between the cavity and the input channel (sometimes the reflection channel), b_{out} is the output field operator at the transmission channel, s_{out} is the output field operator representing spontaneous emission, and $\xi_\gamma(t)$ and $\xi_l(t)$ are input noise operators for the emitter and the cavity.

In the weak excitation regime (i.e., $\langle\sigma_z\rangle \simeq -1$ and $a\sigma_z = -a$) [69] and in the steady state ($\langle\dot{a}\rangle = \langle\dot{\sigma}_{\mathrm{ge}}\rangle = 0$), we find

$$\langle a\rangle = \frac{-\sqrt{\kappa_e}\langle a_{\mathrm{in}}\rangle}{i\Delta_c + \frac{\kappa}{2} + \frac{g^2}{i\Delta_a + \frac{\gamma_0}{2}}}, \tag{J3a}$$

$$\langle\sigma_{\mathrm{ge}}\rangle = \frac{-ig\langle a\rangle}{i\Delta_a + \frac{\gamma_0}{2}}. \tag{J3b}$$

In the absence of dephasing, it can be proven that the magnitudes of the reflection, transmission, and scattering from the system can be simplified to [70]

$$R := \frac{\langle a_{\mathrm{out}}^\dagger a_{\mathrm{out}}\rangle}{\langle a_{\mathrm{in}}^\dagger a_{\mathrm{in}}\rangle} = \left|\frac{\langle a_{\mathrm{out}}\rangle}{\langle a_{\mathrm{in}}\rangle}\right|^2, \tag{J4a}$$

$$T := \frac{\langle b_{\mathrm{out}}^\dagger b_{\mathrm{out}}\rangle}{\langle a_{\mathrm{in}}^\dagger a_{\mathrm{in}}\rangle} = \left|\frac{\langle b_{\mathrm{out}}\rangle}{\langle a_{\mathrm{in}}\rangle}\right|^2, \tag{J4b}$$

$$S := \frac{\langle s_{\mathrm{out}}^\dagger s_{\mathrm{out}}\rangle}{\langle a_{\mathrm{in}}^\dagger a_{\mathrm{in}}\rangle} = \left|\frac{\langle s_{\mathrm{out}}\rangle}{\langle a_{\mathrm{in}}\rangle}\right|^2. \tag{J4c}$$

From Eqs. (J3), the reflection, transmission, and scattering amplitudes take the form

$$r := \frac{\langle a_{\text{out}}\rangle}{\langle a_{\text{in}}\rangle} = 1 - \frac{\kappa_e}{i\Delta_c + \frac{\kappa}{2} + \frac{g^2}{i\Delta_a + \frac{\gamma_0}{2}}}, \tag{J5a}$$

$$t := \frac{\langle b_{\text{out}}\rangle}{\langle a_{\text{in}}\rangle} = -\frac{\sqrt{\kappa_e \kappa_i}}{i\Delta_c + \frac{\kappa}{2} + \frac{g^2}{i\Delta_a + \frac{\gamma_0}{2}}}, \tag{J5b}$$

$$s := \frac{\langle s_{\text{out}}\rangle}{\langle a_{\text{in}}\rangle} = \frac{ig\sqrt{\kappa_e \gamma_0}}{(i\Delta_c + \frac{\kappa}{2})(i\Delta_a + \frac{\gamma_0}{2}) + g^2}. \tag{J5c}$$

The scattering intensity $S(\Delta_a)$ presents a maximum approximately at

$$\Delta_{a,\max} = \frac{-g^2\Delta}{\Delta^2 + \kappa^2/4}, \tag{J6}$$

where $\Delta := w_c - w_a$. The accuracy of the approximation decreases the higher the cooperativity. In Fig. 16, we plot the scattering intensity both as a function of Δ_a and Δ. We see that the peak intensity decreases as the cavity goes into resonance with the emitter. We use this peak intensity envelope function as the fit in Fig. 4(d). The variation in the frequency of the peak intensity cannot be observed in the raw data in Fig. 19(a) due to the inherent spectral diffusion and jumps of the emitter.

Without making assumptions about the emitter excitation regime, but assuming a large total cavity decay rate κ, it can be shown that [69,71]

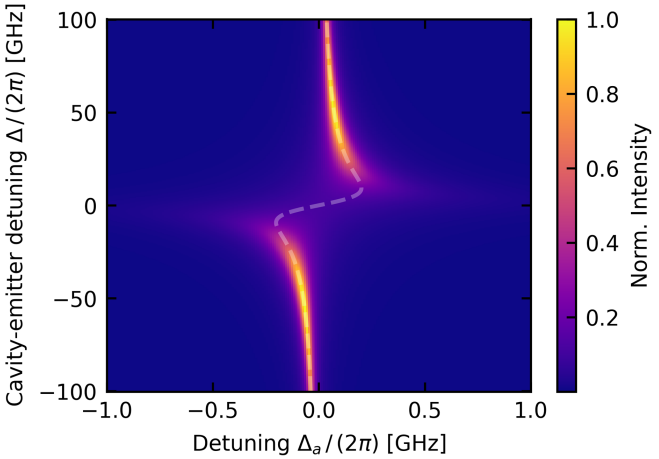

FIG. 16. Normalized scattering intensity $|s|^2$ from Eq. (J5c) as a function of laser-emitter detuning Δ_a and cavity-emitter detuning Δ. The dashed line corresponds to an approximation of the frequency of brightest emission as given by Eq. (J6). For this plot, we use $\{g, \kappa, \gamma_0\}/2\pi = \{1.94, 18.7, 0.02437\}$ GHz.

$$\langle \dot{\sigma_{\text{ge}}}\rangle = -\frac{\gamma_0}{2}\left(1 + i\frac{2\Delta_a}{\gamma_0} + \frac{C}{1 + i\frac{2\Delta_c}{\kappa}}\right)\langle \sigma_{\text{ge}}\rangle - i\frac{\gamma_0}{2}\frac{Y}{1 + i\frac{2\Delta_c}{\kappa}}\langle \sigma_z\rangle, \tag{J7a}$$

$$\langle \dot{\sigma_z}\rangle = -\gamma_0\left(1 + \frac{C}{1 + (\frac{2\Delta_c}{\kappa})^2}\right)(1 + \langle \sigma_z\rangle) + i\gamma_0\left(\frac{Y}{1 + i\frac{2\Delta_c}{\kappa}}\langle \sigma^\dagger_{\text{ge}}\rangle - \frac{Y^*}{1 - i\frac{2\Delta_c}{\kappa}}\langle \sigma_{\text{ge}}\rangle\right), \tag{J7b}$$

where $C = [(4g^2)/(\kappa\gamma_0)]$ and $Y = 4g\sqrt{\kappa_e}\langle a_{\text{in}}\rangle/(\kappa\gamma_0)$. These are the optical Bloch equations of a two-level emitter but with different decay and excitation rates due to the interaction with the cavity. In particular, we see that when the emitter is in resonance with the laser (i.e., $\Delta_a = 0$), the total decay rate γ_0' of the excited-state population follows a Lorentzian with respect to the cavity-emitter detuning,

$$\gamma_0'(\Delta) = (Cf(\Delta) + 1)\gamma_0, \tag{J8}$$

where $f(\Delta) = 1/(1 + 4\Delta^2/\kappa^2)$, which is typically called Purcell enhancement.

APPENDIX K: REFLECTION MEASUREMENTS

To measure the loss rate into the waveguide κ_e, we perform reflection measurements. The reflectivity of a bare cavity can be described by

$$R(\Delta_c) = \left|1 - \frac{\kappa_e}{\kappa/2 + i\Delta_c}\right|^2, \tag{K1}$$

where κ is the total loss rate and $\Delta_c = \omega - \omega_c$ is the detuning between the probe laser and the cavity. From Appendix G, we know that the cavities are undercoupled with $\kappa_e < \kappa/2$. Fitting the cavity reflection under this constraint gives $\kappa_e/\kappa = 0.21$ for Cavity 1 and $\kappa_e/\kappa = 0.31$ for Cavity 2. Because of the lensed fiber configuration, we have significant reflections off the fiber tip [11]. To remove this effect from the measurement, we fit $R'(\Delta_c) = AR(\Delta_c) + c$, where A is an amplitude and c is a constant background that is measured with the fiber far away from the cavity. We measure $c = 21.9$ kHz for Fig. 17(a) and $c = 20.4$ kHz for Fig. 17(b). The maximum reflection counts are around 350 kHz for Cavity 1 and around 750 kHz for Cavity 2.

APPENDIX L: C-QED PARAMETERS

In Table V, we gather all the relevant parameters for both of the investigated devices, together with their source. Note that some of the values are not perfectly consistent. For example, we could also calculate g for Cavity 1 as $g = \sqrt{C\kappa\gamma_0/4} = 1.54$ GHz. This inconsistency is mainly

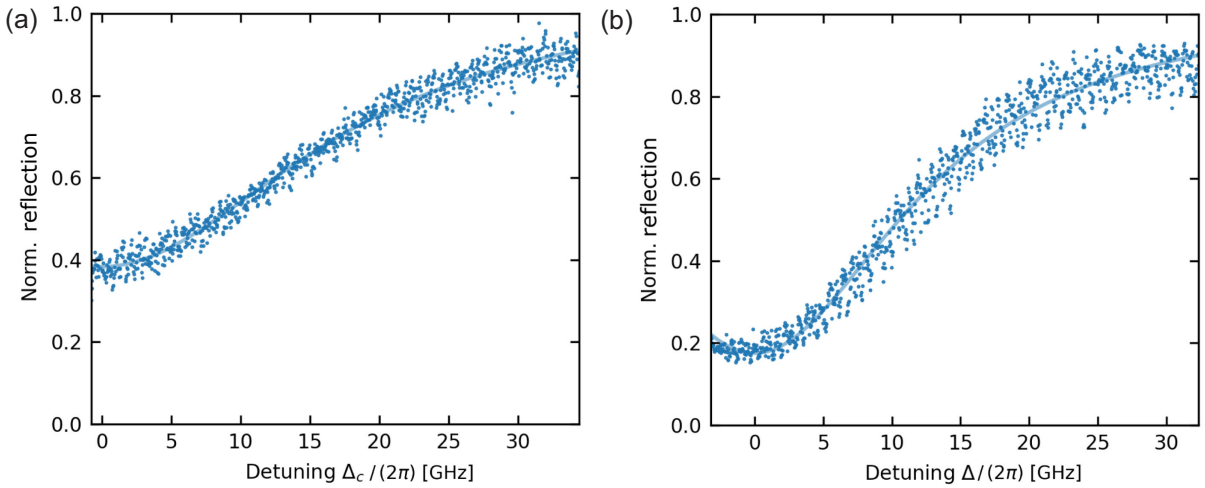

FIG. 17. Cavity reflection measured for Cavity 1 (a) and Cavity 2 (b). The data are fit with $R(\Delta_c) = |1 - [\kappa_e/(\kappa/2 + i\Delta_c)]|^2$ to obtain the out-coupling ratio $\kappa_e/\kappa = 0.21$ for Cavity 1 and $\kappa_e/\kappa = 0.31$ for Cavity 2.

because quality factors can vary from experiment to experiment. We attribute this change to the way the nitrogen gas is deposited on the cavities and then melted away for the frequency tuning. The laser removes ice only locally, leading to an inhomogeneous ice layer and thus degrading the quality factor. The exact quality factor depends on how far and by what means the cavity was tuned and back tuned for a specific measurement.

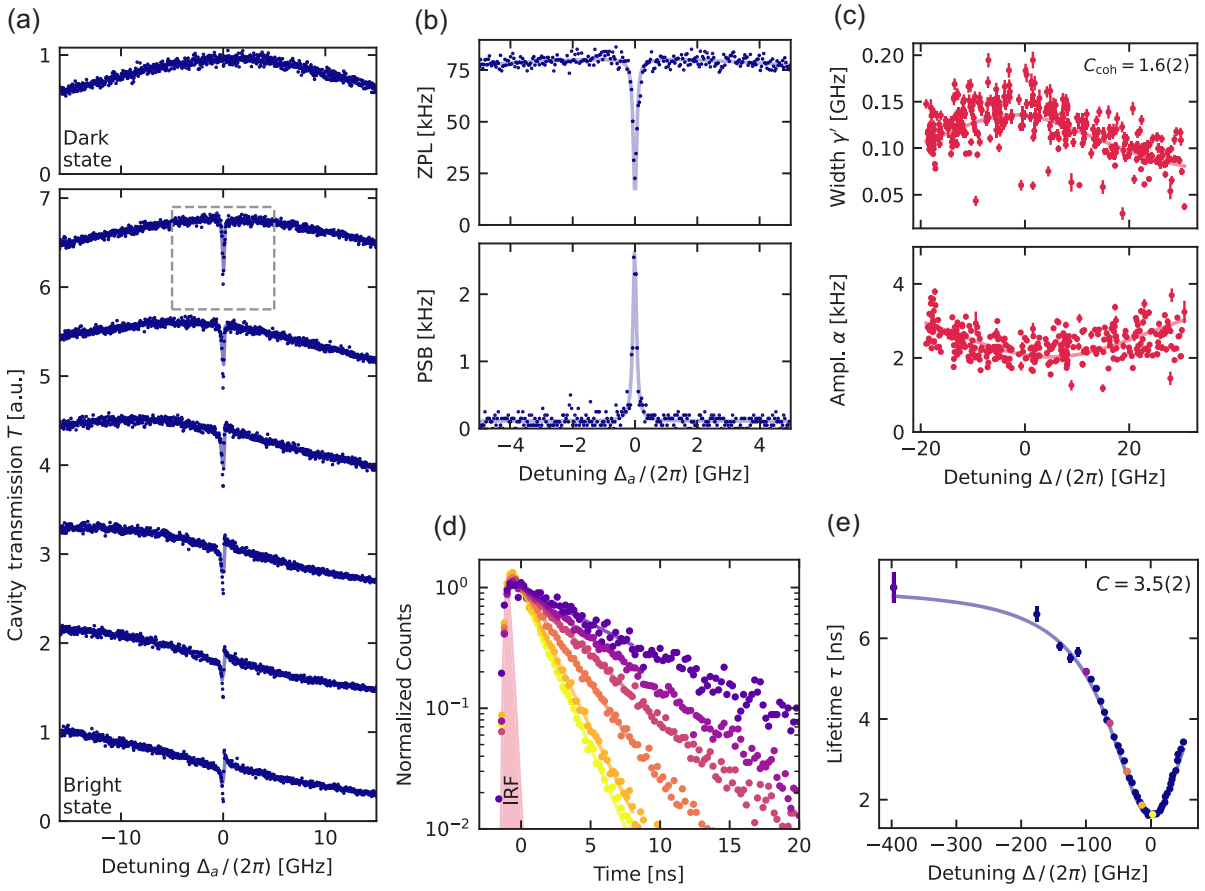

FIG. 18. Device-2 C-QED characterization. (a)–(c) Cavity transmission measurements. In panel (a), the transmission is shown for six different detunings, $\Delta \in [17.2, 15.7, 12.5, 8.9, 5.1, 0.1]$ GHz (for details, see Fig. 4). (d),(e) Lifetime measurements (for details, see Fig. 3). The error bars indicate $\pm 1\sigma$ uncertainty in the fit.

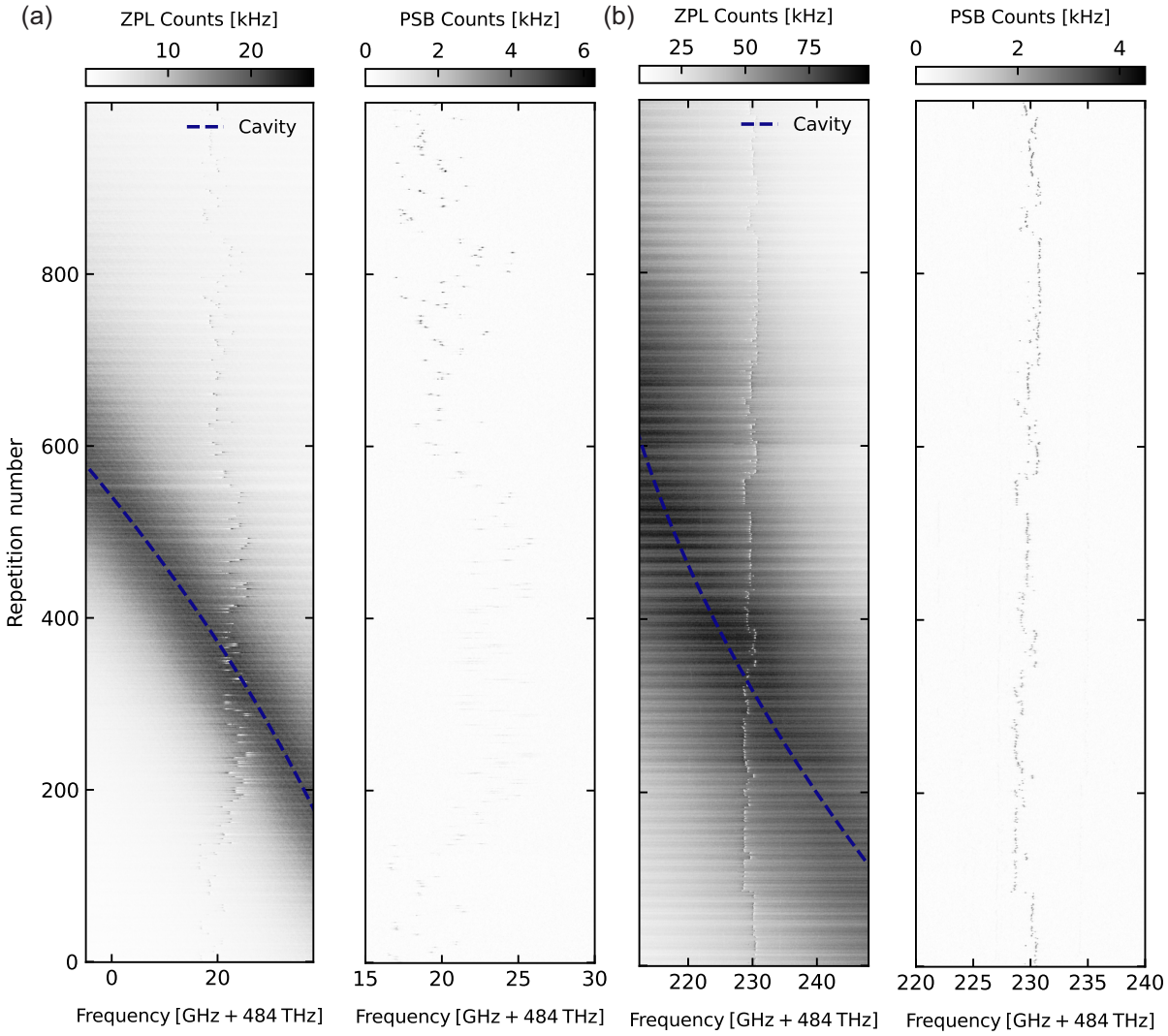

FIG. 19. Complete set of transmission measurements for Cavity 1 (a) and Cavity 2 (b). The cavity red detunes slowly over time due to a small leak in the cryostat.

APPENDIX M: CAVITY-2 DATA

We have performed the full set of C-QED characterizations for a second cavity. This cavity has only one mirror hole in the out-coupling mirror region compared to four mirror holes for Cavity 1. Based on the simulations of Appendix G, we expect Cavity 2 to have a higher out-coupling rate κ_e, comparable intrinsic losses κ_i, and thus a lower overall quality factor. The reflection measurement (Fig. 17) shows that the out-coupling rate is indeed higher (14.5 GHz vs 4.07 GHz). However, the intrinsic losses are also significantly higher (14.9 GHz vs 33 GHz). Figures 18(a)–18(c) show the cavity transmission measurements, and Figs. 18(d) and 18(e) show the lifetime measurements. The C-QED parameters extracted from the transmission measurements are $\{g, \kappa, \gamma\}/2\pi = \{0.99(7), 47.5(21), 0.0537(11)\}$ GHz

[1] H. J. Kimble, *The quantum internet*, Nature (London) **453**, 1023 (2008).
[2] S. Wehner, D. Elkouss, and R. Hanson, *Quantum internet: A vision for the road ahead*, Science **362**, eaam9288 (2018).
[3] D. Gottesman, T. Jennewein, and S. Croke, *Longer-baseline telescopes using quantum repeaters*, Phys. Rev. Lett. **109**, 070503 (2012).
[4] M. Pompili, S. L. N. Hermans, S. Baier, H. K. C. Beukers, P. C. Humphreys, R. N. Schouten, R. F. L. Vermeulen, M. J. Tiggelman, L. d. S. Martins, B. Dirkse, S. Wehner, and R. Hanson, *Realization of a multinode quantum network of remote solid-state qubits*, Science **372**, 259 (2021).
[5] S. L. N. Hermans, M. Pompili, H. K. C. Beukers, S. Baier, J. Borregaard, and R. Hanson, *Qubit teleportation between non-neighbouring nodes in a quantum network*, Nature (London) **605**, 663 (2022).

[6] Y.-C. Wei, P.-J. Stas, A. Suleymanzade, G. Baranes, F. Machado, Y. Q. Huan, C. M. Knaut, S. W. Ding, M. Merz, E. N. Knall, U. Yazlar, M. Sirotin, I. W. Wang, B. Machielse, S. F. Yelin, J. Borregaard, H. Park, M. Lončar, and M. D. Lukin, *Universal distributed blind quantum computing with solid-state qubits*, Science **388**, 509 (2025).

[7] A. J. Stolk *et al.*, *Metropolitan-scale heralded entanglement of solid-state qubits*, Sci. Adv. **10**, eadp6442 (2024).

[8] C. M. Knaut, A. Suleymanzade, Y.-C. Wei, D. R. Assumpcao, P.-J. Stas, Y. Q. Huan, B. Machielse, E. N. Knall, M. Sutula, G. Baranes, N. Sinclair, C. De-Eknamkul, D. S. Levonian, M. K. Bhaskar, H. Park, M. Lončar, and M. D. Lukin, *Entanglement of nanophotonic quantum memory nodes in a telecom network*, Nature (London) **629**, 573 (2024).

[9] A. Sipahigil, R. E. Evans, D. D. Sukachev, M. J. Burek, J. Borregaard, M. K. Bhaskar, C. T. Nguyen, J. L. Pacheco, H. A. Atikian, C. Meuwly, R. M. Camacho, F. Jelezko, E. Bielejec, H. Park, M. Lončar, and M. D. Lukin, *An integrated diamond nanophotonics platform for quantum-optical networks*, Science **354**, 847 (2016).

[10] R. A. Parker, J. Arjona Martínez, K. C. Chen, A. M. Stramma, I. B. Harris, C. P. Michaels, M. E. Trusheim, M. Hayhurst Appel, C. M. Purser, W. G. Roth, D. Englund, and M. Atatüre, *A diamond nanophotonic interface with an optically accessible deterministic electronuclear spin register*, Nat. Photonics **18**, 156 (2024).

[11] M. Pasini, N. Codreanu, T. Turan, A. Riera Moral, C. F. Primavera, L. De Santis, H. K. C. Beukers, J. M. Brevoord, C. Waas, J. Borregaard, and R. Hanson, *Nonlinear quantum photonics with a tin-vacancy center coupled to a one-dimensional diamond waveguide*, Phys. Rev. Lett. **133**, 023603 (2024).

[12] S. W. Ding, M. Haas, X. Guo, K. Kuruma, C. Jin, Z. Li, D. D. Awschalom, N. Delegan, F. J. Heremans, A. A. High, and M. Loncar, *High-Q cavity interface for color centers in thin film diamond*, Nat. Commun. **15**, 6358 (2024).

[13] A. E. Rugar, J. Vuckovic, N. A. Melosh, and Z.-X. Shen, *Quantum photonics with the tin-vacancy center in diamond*, Ph.D. thesis, Stanford University, Department of Applied Physics, and [Stanford University], https://purl.stanford.edu/dd318tr4151.

[14] K. Kuruma, B. Pingault, C. Chia, D. Renaud, P. Hoffmann, S. Iwamoto, C. Ronning, and M. Lončar, *Coupling of a single tin-vacancy center to a photonic crystal cavity in diamond*, Appl. Phys. Lett. **118**, 230601 (2021).

[15] A. Reiserer and G. Rempe, *Cavity-based quantum networks with single atoms and optical photons*, Rev. Mod. Phys. **87**, 1379 (2015).

[16] H. K. Beukers, M. Pasini, H. Choi, D. Englund, R. Hanson, and J. Borregaard, *Remote-entanglement protocols for stationary qubits with photonic interfaces*, PRX Quantum **5**, 010202 (2024).

[17] X. Guo *et al.*, *Microwave-based quantum control and coherence protection of tin-vacancy spin qubits in a strain-tuned diamond-membrane heterostructure*, Phys. Rev. X **13**, 041037 (2023).

[18] E. I. Rosenthal, C. P. Anderson, H. C. Kleidermacher, A. J. Stein, H. Lee, J. Grzesik, G. Scuri, A. E. Rugar, D. Riedel, S. Aghaeimeibodi, G. H. Ahn, K. Van Gasse, and J. Vučković, *Microwave spin control of a tin-vacancy qubit in diamond*, Phys. Rev. X **13**, 031022 (2023).

[19] I. Karapatzakis, J. Resch, M. Schrodin, P. Fuchs, M. Kieschnick, J. Heupel, L. Kussi, C. Sürgers, C. Popov, J. Meijer, C. Becher, W. Wernsdorfer, and D. Hunger, *Microwave control of the tin-vacancy spin qubit in diamond with a superconducting waveguide*, Phys. Rev. X **14**, 031036 (2024).

[20] J. Resch, I. Karapatzakis, M. Elshorbagy, M. Schrodin, P. Fuchs, P. Graßhoff, L. Kussi, C. Sürgers, C. Popov, C. Becher, W. Wernsdorfer, and D. Hunger, *High-fidelity control of a ^{13}C nuclear spin coupled to a tin-vacancy center in diamond*, Phys. Rev. X **16**, 011060 (2026).

[21] H. K. C. Beukers, C. Waas, M. Pasini, H. B. Van Ommen, Z. Ademi, M. Iuliano, N. Codreanu, J. M. Brevoord, T. Turan, T. H. Taminiau, and R. Hanson, *Control of solid-state nuclear spin qubits using an electron spin-1/2*, Phys. Rev. X **15**, 021011 (2025).

[22] N. H. Wan, T.-J. Lu, K. C. Chen, M. P. Walsh, M. E. Trusheim, L. De Santis, E. A. Bersin, I. B. Harris, S. L. Mouradian, I. R. Christen, E. S. Bielejec, and D. Englund, *Large-scale integration of artificial atoms in hybrid photonic circuits*, Nature (London) **583**, 226 (2020).

[23] K. C. Chen, I. Christen, H. Raniwala, M. Colangelo, L. De Santis, K. Shtyrkova, D. Starling, R. Murphy, L. Li, K. Berggren, P. B. Dixon, M. Trusheim, and D. Englund, *A scalable cavity-based spin–photon interface in a photonic integrated circuit*, Opt. Quantum **2**, 124 (2024).

[24] L. Li, L. D. Santis, I. B. W. Harris, K. C. Chen, Y. Gao, I. Christen, H. Choi, M. Trusheim, Y. Song, C. Errando-Herranz, J. Du, Y. Hu, G. Clark, M. I. Ibrahim, G. Gilbert, R. Han, and D. Englund, *Heterogeneous integration of spin–photon interfaces with a CMOS platform*, Nature (London) **630**, 70 (2024).

[25] G. Clark, H. Raniwala, M. Koppa, K. Chen, A. Leenheer, M. Zimmermann, M. Dong, L. Li, Y. H. Wen, D. Dominguez, M. Trusheim, G. Gilbert, M. Eichenfield, and D. Englund, *Nanoelectromechanical control of spin–photon interfaces in a hybrid quantum system on chip*, Nano Lett. **24**, 1316 (2024).

[26] J. M. Brevoord, L. G. C. Wienhoven, N. Codreanu, T. Ishiguro, E. Van Leeuwen, M. Iuliano, L. De Santis, C. Waas, H. K. C. Beukers, T. Turan, C. Errando-Herranz, K. Kawaguchi, and R. Hanson, *Large-range tuning and stabilization of the optical transition of diamond tin-vacancy centers by in situ strain control*, Appl. Phys. Lett. **126**, 174001 (2025).

[27] J. Arjona Martínez, R. A. Parker, K. C. Chen, C. M. Purser, L. Li, C. P. Michaels, A. M. Stramma, R. Debroux, I. B. Harris, M. Hayhurst Appel, E. C. Nichols, M. E. Trusheim, D. A. Gangloff, D. Englund, and M. Atatüre, *Photonic indistinguishability of the tin-vacancy center in nanostructured diamond*, Phys. Rev. Lett. **129**, 173603 (2022).

[28] V. Bushmakin, O. von Berg, C. Sauerzapf, S. Jayaram, A. Denisenko, V. Vorobyov, I. Gerhardt, D. Liu, and J. Wrachtrup, *Two-photon interference of photons from remote tin-vacancy centers in diamond*, arXiv:2412.17539.

[29] J. M. Brevoord, J. F. Geus, T. Turan, M. G. Romero, D. B. Rodríguez, N. Codreanu, A. M. Stramma, R. Hanson, F. Elsen, and B. Jungbluth, *Quantum frequency conversion of*

single photons from a tin-vacancy center in diamond, Opt. Quantum **3**, 583 (2025).

[30] A. E. Rugar, S. Aghaeimeibodi, D. Riedel, C. Dory, H. Lu, P. J. McQuade, Z.-X. Shen, N. A. Melosh, and J. Vučković, *Quantum photonic interface for tin-vacancy centers in diamond*, Phys. Rev. X **11**, 031021 (2021).

[31] Y. Herrmann, J. Fischer, J. M. Brevoord, C. Sauerzapf, L. G. C. Wienhoven, L. J. Feije, M. Pasini, M. Eschen, M. Ruf, M. J. Weaver, and R. Hanson, *Coherent coupling of a diamond tin-vacancy center to a tunable open microcavity*, Phys. Rev. X **14**, 041013 (2024).

[32] S. Mosor, J. Hendrickson, B. C. Richards, J. Sweet, G. Khitrova, H. M. Gibbs, T. Yoshie, A. Scherer, O. B. Shchekin, and D. G. Deppe, *Scanning a photonic crystal slab nanocavity by condensation of xenon*, Appl. Phys. Lett. **87**, 141105 (2005).

[33] K. Srinivasan and O. Painter, *Optical fiber taper coupling and high-resolution wavelength tuning of microdisk resonators at cryogenic temperatures*, Appl. Phys. Lett. **90**, 031114 (2007).

[34] J. Borregaard, A. S. Sørensen, and P. Lodahl, *Quantum networks with deterministic spin–photon interfaces*, Adv. Quantum Technol. **2**, 1800091 (2019).

[35] C. T. Nguyen, D. D. Sukachev, M. K. Bhaskar, B. Machielse, D. S. Levonian, E. N. Knall, P. Stroganov, C. Chia, M. J. Burek, R. Riedinger, H. Park, M. Lončar, and M. D. Lukin, *An integrated nanophotonic quantum register based on silicon-vacancy spins in diamond*, Phys. Rev. B **100**, 165428 (2019).

[36] B. Khanaliloo, M. Mitchell, A. C. Hryciw, and P. E. Barclay, *High-Q/V monolithic diamond microdisks fabricated with quasi-isotropic etching*, Nano Lett. **15**, 5131 (2015).

[37] M. Mitchell, D. P. Lake, and P. E. Barclay, *Realizing* $Q > 300\,000$ *in diamond microdisks for optomechanics via etch optimization*, APL Photonics **4**, 016101 (2019).

[38] S. Mouradian, N. H. Wan, T. Schröder, and D. Englund, *Rectangular photonic crystal nanobeam cavities in bulk diamond*, Appl. Phys. Lett. **111**, 021103 (2017).

[39] M. T. Ruf, *Cavity-enhanced quantum network nodes in diamond*, Doctoral thesis, Delft University of Technology, 2021, 10.4233/uuid:933b37d4-7f00-4070-becc-9c462bf9d8df.

[40] N. Codreanu, *Diamond nanophotonic devices for quantum networks experiments*, Doctoral thesis, Delft University of Technology, 2025, 10.4233/uuid:e1c789d7-d71e-42b8-a9a8-23fafdaea22e.

[41] T. Iwasaki, Y. Miyamoto, T. Taniguchi, P. Siyushev, M. H. Metsch, F. Jelezko, and M. Hatano, *Tin-vacancy quantum emitters in diamond*, Phys. Rev. Lett. **119**, 253601 (2017).

[42] J. Görlitz, D. Herrmann, G. Thiering, P. Fuchs, M. Gandil, T. Iwasaki, T. Taniguchi, M. Kieschnick, J. Meijer, M. Hatano, A. Gali, and C. Becher, *Spectroscopic investigations of negatively charged tin-vacancy centres in diamond*, New J. Phys. **22**, 013048 (2020).

[43] J. Borregaard, P. Kómár, E. M. Kessler, M. D. Lukin, and A. S. Sørensen, *Long-distance entanglement distribution using individual atoms in optical cavities*, Phys. Rev. A **92**, 012307 (2015).

[44] E. N. Knall, C. M. Knaut, R. Bekenstein, D. R. Assumpcao, P. L. Stroganov, W. Gong, Y. Q. Huan, P.-J. Stas, B. Machielse, M. Chalupnik, D. Levonian, A. Suleymanzade, R. Riedinger, H. Park, M. Lončar, M. K. Bhaskar, and M. D. Lukin, *Efficient source of shaped single photons based on an integrated diamond nanophotonic system*, Phys. Rev. Lett. **129**, 053603 (2022).

[45] J. Görlitz, D. Herrmann, P. Fuchs, T. Iwasaki, T. Taniguchi, D. Rogalla, D. Hardeman, P.-O. Colard, M. Markham, M. Hatano, and C. Becher, *Coherence of a charge stabilised tin-vacancy spin in diamond*, npj Quantum Inf. **8**, 45 (2022).

[46] P. Wang, L. Kazak, K. Senkalla, P. Siyushev, R. Abe, T. Taniguchi, S. Onoda, H. Kato, T. Makino, M. Hatano, F. Jelezko, and T. Iwasaki, *Transform-limited photon emission from a lead-vacancy center in diamond above 10 K*, Phys. Rev. Lett. **132**, 073601 (2024).

[47] A. Ruskuc, C.-J. Wu, E. Green, S. L. N. Hermans, W. Pajak, J. Choi, and A. Faraon, *Multiplexed entanglement of multi-emitter quantum network nodes*, Nature (London) **639**, 54 (2025).

[48] J. M. Bopp, M. Plock, T. Turan, G. Pieplow, S. Burger, and T. Schröder, *'Sawfish' Photonic crystal cavity for near-unity emitter-to-fiber interfacing in quantum network applications*, Adv. Opt. Mater. **12**, 2301286 (2024).

[49] X. Guo, M. Xie, A. Addhya, A. Linder, U. Zvi, S. Wang, X. Yu, T. D. Deshmukh, Y. Liu, I. N. Hammock, Z. Li, C. T. DeVault, A. Butcher, A. P. Esser-Kahn, D. D. Awschalom, N. Delegan, P. C. Maurer, F. J. Heremans, and A. A. High, *Direct-bonded diamond membranes for heterogeneous quantum and electronic technologies*, Nat. Commun. **15**, 8788 (2024).

[50] X. Guo, N. Delegan, J. C. Karsch, Z. Li, T. Liu, R. Shreiner, A. Butcher, D. D. Awschalom, F. J. Heremans, and A. A. High, *Tunable and transferable diamond membranes for integrated quantum technologies*, Nano Lett. **21**, 10392 (2021).

[51] S. W. Ding, C. Jin, K. Kuruma, X. Guo, M. Haas, B. Korzh, A. Beyer, M. D. Shaw, N. Sinclair, D. D. Awschalom, F. J. Heremans, N. Delegan, A. A. High, and M. Loncar, *Purcell-enhanced emissions from diamond color centers in slow light photonic crystal waveguides*, Nano Lett. **25**, 12125 (2025).

[52] B. Zeng, C. De-Eknamkul, D. Assumpcao, D. Renaud, Z. Wang, D. Riedel, J. Ha, C. Robens, D. Levonian, M. Lukin, R. Riedinger, M. Bhaskar, D. Sukachev, M. Loncar, and B. Machielse, *Cryogenic packaging of nanophotonic devices with a low coupling loss* < 1 dB, Appl. Phys. Lett. **123**, 161106 (2023).

[53] T. Schröder, M. E. Trusheim, M. Walsh, L. Li, J. Zheng, M. Schukraft, A. Sipahigil, R. E. Evans, D. D. Sukachev, C. T. Nguyen *et al.*, *Scalable focused ion beam creation of nearly lifetime-limited single quantum emitters in diamond nanostructures*, Nat. Commun. **8**, 1 (2017).

[54] M. J. Burek, N. P. de Leon, B. J. Shields, B. J. M. Hausmann, Y. Chu, Q. Quan, A. S. Zibrov, H. Park, M. D. Lukin, and M. Lončar, *Free-standing mechanical and photonic nanostructures in single-crystal diamond*, Nano Lett. **12**, 6084 (2012).

[55] X. Cheng, A. Thurn, G. Chen, G. S. Jones, J. E. Bennett, M. Coke, M. Adshead, C. P. Michaels, O. Balci, A. C. Ferrari, M. Atatüre, R. J. Curry, J. M. Smith, P. S. Salter, and D. A. Gangloff, *Laser activation of single group-IV colour centres in diamond*, Nat. Commun. **16**, 5124 (2025).

[56] J. M. Brevoord, L. De Santis, T. Yamamoto, M. Pasini, N. Codreanu, T. Turan, H. K. Beukers, C. Waas, and R. Hanson, *Heralded initialization of charge state and optical-transition frequency of diamond tin-vacancy centers*, Phys. Rev. Appl. **21**, 054047 (2024).

[57] J. D. Hood, A. Goban, A. Asenjo-Garcia, M. Lu, S.-P. Yu, D. E. Chang, and H. J. Kimble, *Atom–atom interactions around the band edge of a photonic crystal waveguide*, Proc. Natl. Acad. Sci. U.S.A. **113**, 10507 (2016).

[58] J. Borregaard, H. Pichler, T. Schröder, M. D. Lukin, P. Lodahl, and A. S. Sørensen, *One-Way quantum repeater based on near-deterministic photon-emitter interfaces*, Phys. Rev. X **10**, 021071 (2020).

[59] N. Codreanu, T. Turan, D. Bedialauneta-Rodriguez, M. Pasini, L. de Santis, M. Ruf, C. F. Primavera, Leonardo G. C. Wienhoven, C. E. Smulders, S. Groblacher, and R. Hanson, *Data underlying the publication "Above-Unity Coherent Cooperativity of Tin-Vacancy Centers in Diamond Photonic Crystal Cavities"* (2025), 10.4121/df7ca98d-f2f3-485c-a91c-12810555321f.v1.

[60] M. J. Burek, C. Meuwly, R. E. Evans, M. K. Bhaskar, A. Sipahigil, S. Meesala, B. Machielse, D. D. Sukachev, C. T. Nguyen, J. L. Pacheco, E. Bielejec, M. D. Lukin, and M. Lončar, *Fiber-coupled diamond quantum nanophotonic interface*, Phys. Rev. Appl. **8**, 024026 (2017).

[61] J. Chan, *Laser cooling of an optomechanical crystal resonator to its quantum ground state of motion, California Institute of Technology* (2012).

[62] J. D. Joannopoulos, S. G. Johnson, J. N. Winn, and R. D. Meade, *Photonic Crystals: Molding the Flow of Light, 2nd edition*, in *Photonic Crystals* (Princeton University Press, Princeton, NJ, 2011).

[63] COMSOL Multiphysics, COMSOL Inc., Stockholm, Sweden (2024), version 6.2.

[64] S. Strauf, M. T. Rakher, I. Carmeli, K. Hennessy, C. Meier, A. Badolato, M. J. A. DeDood, P. M. Petroff, E. L. Hu, E. G. Gwinn, and D. Bouwmeester, *Frequency control of photonic crystal membrane resonators by monolayer deposition*, Appl. Phys. Lett. **88**, 043116 (2006).

[65] D. Dalacu, K. Mnaymneh, V. Sazonova, P. J. Poole, G. C. Aers, R. Cheriton, M. Reimer, J. Lapointe, P. Hawrylak, M. Korkusiński, E. Kadantsev, and R. Williams, *Scalable routes to single and entangled photon pair sources: Tailored InAs/InP quantum dots in photonic crystal microcavities*, Quantum Sens. Nanophotonic Devices VII **7608**, 758 (2010).

[66] R. E. Evans, M. K. Bhaskar, D. D. Sukachev, C. T. Nguyen, A. Sipahigil, M. J. Burek, B. Machielse, G. H. Zhang, A. S. Zibrov, E. Bielejec, H. Park, M. Lončar, and M. D. Lukin, *Photon-mediated interactions between quantum emitters in a diamond nanocavity*, Science **362**, 662 (2018).

[67] N. Lettner, L. Antoniuk, A. P. Ovvyan, H. Gehring, D. Wendland, V. N. Agafonov, W. H. P. Pernice, and A. Kubanek, *Controlling all degrees of freedom of the optical coupling in hybrid quantum photonics*, ACS Photonics **11**, 696 (2024).

[68] C. W. Gardiner and M. J. Collett, *Input and output in damped quantum systems: Quantum stochastic differential equations and the master equation*, Phys. Rev. A **31**, 3761 (1985).

[69] T. G. Tiecke, J. D. Thompson, N. P. De Leon, L. R. Liu, V. Vuletić, and M. D. Lukin, *Nanophotonic quantum phase switch with a single atom*, Nature (London) **508**, 241 (2014).

[70] B. Julsgaard and K. Mølmer, *Reflectivity and transmissivity of a cavity coupled to two-level systems: Coherence properties and the influence of phase decay*, Phys. Rev. A **85**, 013844 (2012).

[71] P. Rice and H. Carmichael, *Single-atom cavity-enhanced absorption. I. Photon statistics in the bad-cavity limit*, IEEE J. Quantum Electron. **24**, 1351 (1988).